A 3D Tractable Model for UAV-Enabled Cellular Networks With Multiple Antennas

Chun-Hung Liu, Senior Member, IEEE, Di-Chun Liang, Md Asif Syed, and Rung-Hung Gau, Senior Member, IEEE

Abstract—This paper aims to propose a three-dimensional (3D) point process that can be employed to generally deploy unmanned aerial vehicles (UAVs) in a large-scale 3D cellular network and to tractably analyze the fundamental network-wide performances of the network. The proposed 3D point process is devised based on a 2D marked Poisson point process in which each point and its random mark uniquely correspond to the projection and the altitude of each point in the 3D point process, respectively. We study some of the important statistical properties of the proposed 3D point process and shed light on some crucial insights into them that facilitate the analyses of a UAV-enabled cellular network wherein all UAVs equipped with multiple antennas are deployed by the proposed 3D point process to serve as aerial base stations. The salient features of the proposed 3D point process lie in its suitability in practical 3D channel modeling and tractability in analysis. The downlink coverages of the UAV-enabled cellular network are found and their closed-form results for some special cases are also derived. Most importantly, their fundamental limits achieved by cell-free massive antenna array are characterized when coordinating all the UAVs to jointly perform non-coherent downlink transmission. These key findings and observations are numerically validated in this paper.

Index Terms—Three-dimensional point process, Poisson point process, unmanned aerial vehicle, cellular network, coverage, cell-free massive MIMO.

I. INTRODUCTION

N recent years, the technology of unmanned aerial vehicle (UAV) has been improved significantly such that UAVs possess an outstanding capability of agilely moving in three-dimensional (3D) space, which has attracted increasing attention from the academia and industry of wireless communications because such a 3D moving capability is able to remarkably relieve spatial limitations, which usually lead to the impairments of wireless channels between two static terminals, such as path loss, penetration loss, and multi-path fading, etc. Qualcomm and AT&T, for example, have been planning to build up a *UAV-enabled cellular network* with UAVs working as "aerial base stations" in order to enable large-scale wireless

Manuscript received July 20, 2020; revised November 5, 2020, December 29, 2020; accepted January 10, 2021. The work of C.-H. Liu and M. A. Syed was supported in part by National Science Foundation under Award CNS-2006453 and in part by Mississippi State University under Grant ORED 253551-060702. The work of D.-C. Liang and R.-H. Gau was supported in part by the Ministry of Science and Technology in Taiwan under grant number MOST 108-2634-F-009-004 and MOST 109-2634-F-009-023. (Corresponding author: Chun-Hung Liu.)

C.-H. Liu and M. A. Syed are with the Department of Electrical and Computer Engineering, Mississippi State University, Starkville, MS 39762, USA. (e-mail: chliu@ece.msstate.edu; ms4273@msstate.edu)

D.-C. Liang and R.-H. Gau are with the Institute of Communications Engineering and Department of Electrical and Computer Engineering, National Chiao Tung University, Hsinchu 30010, Taiwan. (e-mail: ldc30108@gmail.com; runghunggau@g2.nctu.edu.tw) communications in the upcoming fifth generation (5G) cellular networks [1]. Moreover, Amazon prime air and Google's drone delivery project are two striking examples of using "cellular-connected" UAV communications where UAVs are aerial mobile users in a cellular network [2]. Although the agile and flexible mobility of UAVs benefits point-to-point communications between UAVs and other terminals, it may not really facilitate communications in a wireless network where many UAVs are arbitrarily deployed and a considerable amount of co-channel interference is created accordingly. As such, how to appropriately deploy UAVs in a wireless network to reap the mobility advantage of UAVs is a prominent problem pertaining to all the aspects of UAV communications and networking.

The 3D deploying problem for a UAV-enabled cellular network with UAVs serving as aerial base stations is involved in the issue of simultaneous multi-user coverage, and thereby it is much more complicated and difficult than the 3D deploying problem for a cellular-connected UAV network that merely needs to tackle the issue of single UAV coverage at a time. Deploying methods for a UAV-enabled cellular network should be able to exploit the mobility of UAVs in order to ameliorate the fundamental coverage limit of the entire cellular network, yet how to evaluate the deploying methods in a tractable and network-wide way remains unclear until now. The key to tackling the problems of deploying and evaluating a UAV-enabled cellular network lies in the tractability of the modeling framework of UAV-enabled cellular networks that certainly depends upon the randomly distributed nature of UAVs hovering in the sky. On account of this, we propose a 3D deployment model for a UAV-enabled cellular network, which is able to not only generally characterize the spatial random distribution of the UAVs in the network, but also skillfully pave a tractable way to analyze the performances of the UAV-enabled cellular network. The 3D deployment model proposed to deploy a UAV-enabled cellular network is devised based on a 3D point process, which is essentially a 2D homogeneous marked Poisson point process (PPP) in that all the projections and the altitudes of the 3D point process respectively consist of all the points and the marks of the 2D homogeneous marked PPP. Such a 3D point process is able to generally and practically characterize the randomly positioning characteristic of UAVs in a large-scale UAV-enabled cellular network so that it is very distinct from the existing UAVrelated deployment models in the literature, as reviewed in the following.

A. Prior Works on Modeling UAV-Enabled Wireless Networks

Many of the prior works on UAV-enabled cellular networks studied their problems by assuming a fixed number of UAVs deployed in the sky (typically see [3]–[8]). References [3]– [5], for example, adopted a single UAV in a wireless network to analyze the performance metrics of the network, such as outage probability, energy efficiency, and throughput, to see how to position a UAV so that the performance metrics can be maximized. The problem of how to jointly optimize the flight radius and speed of a single UAV so as to maximize the energy efficiency of a UAV was tackled in [6], whereas the problem of how to use a variable-rate relaying approach to optimizing outage probability and information rate for a single UAV was studied in [7]. Reference [8] analyzed the link capacity for two UAVs with random 3D trajectories and then addressed the impacts of network densification, imperfect channel state information, and interference on the link capacity. Although the modeling and analysis approaches of these prior works seem suitable for a wireless network with a small number of UAVs, in general they cannot be straightforwardly employed in large-scale UAV-enabled wireless networks, which need to take into account of the interactions between UAVs.

There are indeed some prior works that modeled UAVenabled wireless networks in a large-scale sense, e.g., [9]-[15]. However, the majority of them simply assumed that all UAVs in a network hover at the same fixed altitude. For example, reference [9] investigated the coverage problem for a finite network model assuming a number of UAVs are uniformly distributed at the same fixed altitude in the network. The coverages based on UAV-centric and user-centric strategies for multi-UAV-assisted NOMA networks were studied in [10]. Reference [11] proposed a UAV-assisted wireless network for the malfunction areas and used a user-centric cooperation scheme to evaluate the coverage and normalized spectral efficiency of the network. A multi-layer UAV network was proposed in [12] to analyze and optimize the successful transmission probability and spectral efficiency of the network, while the coverage and ergodic rate of a UAV-enabled network were investigated with a spectrum sharing mechanism in [13]. These prior works all assumed that all UAVs hover at the same fixed altitude in a network so that their analyses cannot practically reflect how they are influenced by a real-world deployment of UAVs with a random altitude.

Some prior works already tried to relax the modeling assumption of "fixed altitude" when modeling multiple UAVs in the sky. Reference [16], for example, studied the coverage probability in a 3D deployment model of UAVs wherein all UAVs were distributed within a specific range of altitude that was uniformly divided into a certain number of levels. Reference [16] considered that UAVs were uniformly distributed above a 2D plane and positioned at different levels of altitude. A few prior works also adopted 3D homogeneous PPPs to model UAV-enabled cellular networks. Reference [17] exploited the limits of the coverage and volume spectral efficiency of a mmWave UAV cellular network in which a UAV's altitude was modeled as a function of the UAV's projection. The coverage and network throughput of a NOMA-

assisted UAV network modeled by a 3D homogeneous PPP were analyzed in [18], whereas reference [19] considered spectrum sharing when analyzing the success probability and total network throughput of a UAV-enabled network modeled by a 3D PPP. Modeling the distribution of UAVs by 3D PPPs entails two practical issues. One is that UAVs are low-altitude platforms and cannot be arbitrarily positioned in infinitely large 3D space modeled by a 3D PPP. The other is that the path-loss exponent of any wireless links in a wireless network modeled by a 3D PPP needs to be greater than three in order to make analysis bounded, yet such a constraint on the path-loss exponent is not practically true for most 3D wireless links with a path-loss exponent smaller than three.

B. Contributions

Although these aforementioned prior works successfully conducted some analyses for specific problems they are interested in, in general their outcomes are not easily generalized to a network-wide scenario in a large-scale UAV-enabled cellular network in that their generality is subject to their simplified models and assumptions of deploying UAVs in a wireless network. Our proposed 3D deployment model for a UAV-enabled cellular network, as will be shown in the following sections, inherits the tractability of employing PPPs to model and analyze a wireless network, offers an additional degree of freedom in controlling the altitude of a UAV, and more importantly fits practical 3D path-loss channel models. Consequently, the analytical results of this paper are more general and closer to practical results in a UAV-enabled cellular network. The main contributions of this paper are summarized as follows.

- A 3D point process is proposed based on a 2D homogeneous *marked* PPP in which each point and its mark are the terrestrial projection and the random altitude of a unique point in the 3D point process, respectively. This 3D point process is shown to work for all practical 3D path-loss channel models between any two points in the point process.
- In the proposed 3D point process, we consider angle-projection-independent locating (APIL) and angle-projection-dependent locating (APDL) scenarios when positioning all the UAVs in the sky. The APIL scenario refers to when the elevation angle and the projection of each UAV are independent, whereas the APDL scenario refers to the opposite. The proposed 3D point process is shown to be essentially a 2D homogeneous PPP in the APIL scenario, yet it is shown to be equivalent to a 2D non-homogeneous PPP in the APDL scenario.
- The fundamental properties of the proposed 3D point process are analyzed for the APIL and APDL scenarios, which facilitate the derivations and analyses of the Laplace transforms of the *complete and truncated* (incomplete) 3D shot signal processes with considering line-of-sight (LoS) and non-line-of-sight (NLoS) channel behaviors.
- The proposed 3D point process is employed to generally model the random deployment of the UAVs that are

3

equipped with multiple antennas and serve as aerial base stations in a large-scale cellular network and the *downlink coverages* (probabilities) for the APIL and APDL scenarios are explicitly found and some of them are shown to reduce to a closed-form expression for special channel conditions.

• The *cell-free downlink coverages* for the APIL and APDL scenarios are explicitly derived when all the UAVs in the network can do non-coherent joint transmission. They represent the fundamental upper limits of the downlink coverage probabilities that are achievable in the two scenarios. Their closed-form expressions for some special channel condition are obtained as well.

Furthermore, we provide numerical results to validate the correctness of the analytical findings of the downlink coverages in this paper and show that in general the downlink coverages are insensitive to the different distributions of the elevation angle and the altitude of UAVs that have the same mean so that they can be approximated by the derived expressions using the mean of the elevation angle of a UAV for APIL and the mean of the altitude of a UAV for APDL.

C. Paper Organization

The rest of this paper is organized as follows. In Section II, a 3D point process is proposed and some of its important statistical properties are studied. We employ the proposed 3D point process to model a 3D UAV-enabled cellular network consisting of a tier of UAVs serving as aerial base stations with multiple antennas and we then analyze the downlink coverage performances of the UAV-enabled cellular network in Section III. Section IV provides some numerical results in order to validate the analytical findings in Section III. Finally, Section V concludes the important findings in this paper.

II. THE PROPOSED 3D POINT PROCESS AND ITS STATISTICAL PROPERTIES

Suppose a 2D homogeneous PPP of density λ can be denoted by the following set on the plane of \mathbb{R}^2

$$\Phi_x \triangleq \{X_i \in \mathbb{R}^2 : i \in \mathbb{N}_+\},\tag{1}$$

and it is assumed to be a *simple* point process, that is, none of the points in Φ_x can have the same location on the plane of \mathbb{R}^2 . In accordance with Φ_x , we propose the following 3D point process Φ_u :

$$\Phi_u \triangleq \left\{ U_i \in \mathbb{R}^2 \times \mathbb{R}_+ : U_i = (X_i, H_i), X_i \in \Phi_x, \right.$$

$$H_i = \|X_i\| \tan(\Theta_i), \Theta_i \in \left[0, \frac{\pi}{2}\right], i \in \mathbb{N}_+ \right\}, \quad (2)$$

where X_i is the projection of point U_i on the plane of \mathbb{R}^2 , $||X_i||$ is the distance between the origin¹ and X_i , and Θ_i is the (random) elevation angle from the origin to point U_i .

 1 Without loss of generality, in this paper we use the origin as a reference point for the locations of the points in point sets such as Φ_x and Φ_u to express their relevant equations, results, and observations. According to the Slivnyak theorem [20] [21], the statistical properties of a PPP evaluated at the origin are the same as those evaluated at any particular point in the PPP.

Hence, the "altitude" of point U_i is H_i that is the distance from X_i to U_i such that Φ_u can be viewed as a marked version of Φ_x in which each point has a mark as its altitude. Since $\|Y_i - Y_j\|$ denotes the Euclidean distance between points Y_i and Y_j for $i \neq j$, we know $\|X_i\| = \|U_i\| \cos(\Theta_i)$ and thus $\|U_i\| = \|X_i\| \sec(\Theta_i)$. A link between two spatial points is called a LoS link provided it is not visually blocked from one point to the other. A low-altitude-platform communication scenario is considered in this paper and the LoS model of a 3D channel in [22] is adopted so that we have the following LoS probability of the 3D channel between the origin and a point $U_i \in \Phi_u$ proposed in [22]:

$$\rho(\Theta_i) \triangleq \frac{1}{1 + c_2 \exp(-c_1 \Theta_i)},\tag{3}$$

where c_1 and c_2 are environment-related positive constants (for rural, urban, etc.), and thereby whether or not point U_i is LoS for the origin is completely determined by its elevation angle Θ_i from the origin.

For the 3D point process Φ_u , we will specifically consider two positioning scenarios for the points in Φ_u , i.e., the angle-projection-independent locating (APIL) and the angleprojection-dependent locating (APDL) scenarios2. An illustration of using the proposed 3D point process Φ_u to deploy UAVs based on these two scenarios is depicted in Fig. 1. In the figure, the projections of the UAVs on the X - Y (ground) plane form a 2D homogeneous PPP Φ_x . In the APIL scenario, as shown in part (a) of the figure, the elevation angle and the projection of each point in Φ_u are independent, that is, Θ_i and X_i are independent for all $i \in \mathbb{N}_+$, and we thus can use Θ_i and X_i to completely define the 3D location of UAV U_i . In contract, part (b) of the figure depicts the APDL scenario in which the altitude and the projection of a UAV are independent so that they can also be adopted to completely describe the 3D location of a UAV. Note that the elevation angle and the projection of a UAV is no longer independent once the altitude and the projection of the UAV are independent because they can be used to find the elevation angle between them, i.e., $\Theta_i = \tan^{-1}(H_i/\|X_i\|)$ for all $i \in \mathbb{N}$. In fact, the APIL scenario corresponds the scenario of employing the 3D polar coordinate system to describe the locations of UAVs, whereas the APDL corresponds to the scenario of employing the Cartesian coordinate system to describe the locations of UAVs. The main motivation of considering the APDL and APDL scenarios in this paper is inspired by the fact that they both have their practical deployment applications. The APIL scenario properly characterizes the deployment situation that when each UAV in Φ_u is positioned at a random ground point and at a random elevation angle whose distribution can be observed at the origin. Such a situation usually happens when there is a ground central controller that adjusts the elevation angle of a UAV so as to make the wireless channel between the UAV and a user more likely to be an LoS one. The APDL scenario appropriately characterizes the situation that when

²Note that the APDL scenario can also be referred to as the *altitude(height)*-projection-independent positioning scenario because the APDL scenario is essentially defined in a way that the altitude and the projection of a point in Φ_u are independent.

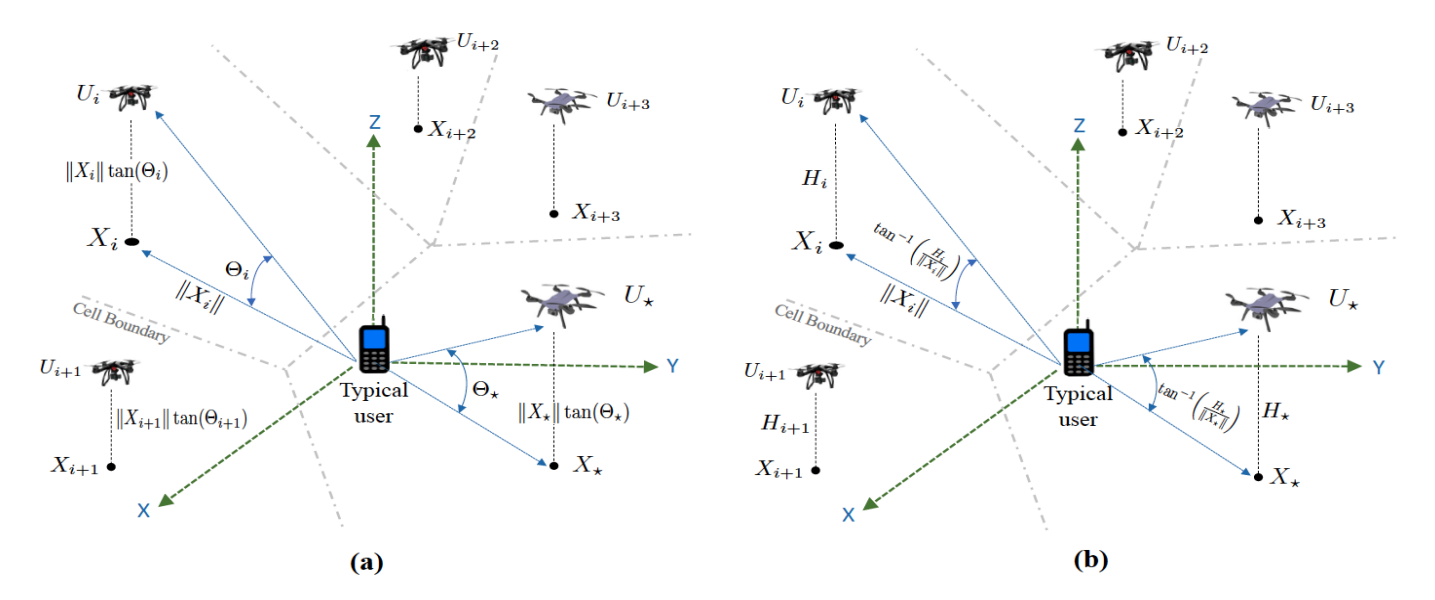


Fig. 1. The proposed 3D point process Φ_u is used to model the locations of the UAVs in a cellular network and the projections of all the points in Φ_u form a 2D homogeneous PPP of density λ on the X - Y plane. The projection of point U_i is denoted by X_i and a typical user located at the origin associates with UAV U_{\star} serving as its aerial base station. Two scenarios of locating the UAVs are considered: (a) The APIL scenario: Θ_i and $\|X_i\|$ are independent for all $i \in \mathbb{N}_+$ and $H_i = \tan(\Theta_i)\|X_i\|$ depends on Θ_i and X_i . (b) The APDL scenario: H_i and $\|X_i\|$ are independent for all $i \in \mathbb{N}_+$ so that $\Theta_i = \tan^{-1}(H_i/\|X_i\|)$ is dependent upon H_i and X_i .

each UAV in Φ_u is positioned at a random projection and at a random altitude whose distribution is known. Such a situation frequently occurs when each point (UAV) in Φ_i is positioned by a ground central controller at a random altitude in accordance with some specific rule. In the following, we will analyze some important statistical properties related to Φ_u by considering these two scenarios.

A. Distance-Related Distributions in Φ_u

Suppose a non-negative RV R_{\star} is defined as

$$R_{\star} \triangleq \max_{i:U_i \in \Phi_u} \left\{ W_i L_i \|U_i\|^{-\alpha} \right\},\tag{4}$$

where $\alpha>2$ is a constant³, $L_i\in\{1,\ell\}$ is a Bernoulli RV that is equal to one if an LoS link between the origin and point U_i exists and ℓ otherwise, and $W_i\in\mathbb{R}_+$ is a nonnegative weighting RV associating with U_i and independent of all L_i 's and U_i 's. Note that $\ell\in[0,1]$ is referred to as the NLoS channel attenuation factor since it is used to model the penetration loss of an NLoS link, W_i is independent of L_j and U_j for all $i,j\in\mathbb{N}_+$, all W_i 's are assumed to be independently and identically distributed (i.i.d.), and the distribution of L_i depends on the location of U_i as indicated by the LoS probability in (3). Throughout this paper, all the evaluation angles in Φ_u are assumed to be i.i.d. for the APIL scenario and all the altitudes in Φ_u are i.i.d. for the APDL scenario. We then have the following theorem.

 $^3 \mathrm{If} \ \|U_i\|^{-\alpha}$ stands for the path loss between node U_i and the origin, α is referred to as the path-loss exponent, which will be used in Section III. Moreover, the channel model adopted in 4 is for wireless channels in the UHF band. For wireless channels in much higher frequency bands (e.g., the mmWave band), a much complicated channel model should be adopted to properly characterize the NLoS effects on the channels, such as the channel models adopted in [17], [23].

Theorem 1. Suppose the moment of W_i exists (i.e., $\mathbb{E}[W_i^a] < \infty$ for all a > 0) for all $i \in \mathbb{N}_+$. (i) If the APIL scenario is considered such that Θ_i and $\|X_j\|$ are independent for all $i, j \in \mathbb{N}_+$ and all Θ_i 's are independently and identically distributed (i.i.d.), the cumulative density function (CDF) of R_{\star} defined in (4) can be found as

$$F_{R_{\star}}(r) = \exp\left(-\pi\lambda \mathbb{E}\left[W^{\frac{2}{\alpha}}\right]\omega r^{-\frac{2}{\alpha}}\right),$$
 (5)

where $F_Z(\cdot)$ denotes the CDF of RV Z and ω is defined as

$$\omega \triangleq \mathbb{E}\left\{\cos^2(\Theta)\left[\rho(\Theta)\left(1 - \ell^{\frac{2}{\alpha}}\right) + \ell^{\frac{2}{\alpha}}\right]\right\}.$$
 (6)

(ii) If the APDL scenario is considered such that $\Theta_i = \tan^{-1}(H_i/\|X_i\|)$ and all H_i 's are i.i.d., then $F_{R_\star}(r)$ can be derived as

$$F_{R_{+}}(r) = \exp\left[-\pi\lambda\Omega\left(r\right)\right],\tag{7}$$

where $\Omega(r)$ is defined as

$$\Omega(r) \triangleq \int_{0}^{\infty} \mathbb{E}_{H} \left\{ \left[\rho(\Theta) F_{W}^{c} \left(r(z + H^{2})^{\frac{\alpha}{2}} \right) + [1 - \rho(\Theta)] F_{W}^{c} \left(\frac{r}{\ell} (z + H^{2})^{\frac{\alpha}{2}} \right) \right] \right\} dz \quad (8)$$

in which $\Theta = \tan^{-1}(H/\sqrt{z})$ and $F_W^c(\cdot)$ denotes the complementary CDF (CCDF) of RV W.

Proof: See Appendix A.

Note that the expression in (7) is more complicated than its corresponding closed-form expression in (5) due to the dependence between the elevation angle Θ_i and the projection X_i of point U_i in Φ_u for all $i \in \mathbb{N}_+$ and it reduces to (5) once the dependence does not exist (Namely, Θ in (8) is not a function of H and z.). Furthermore, in general ω in (6) is insensitive to the different distributions of Θ that have the

same mean, especially when the mean of Θ is not very large. This point will be numerically demonstrated in Section IV-A.

The results in (5) and (7) are very general since they are valid for the general distributions of W and Θ . Accordingly, they can be employed to find the distributions of some specific RVs related to set Φ_u . To demonstrate this, we discuss some special cases of R_{\star} in the following.

1) $W_i = L_i = 1$: In this case, R_\star in (4) reduces to $R_\star = \max_{U_i \in \Phi_u} \|U_i\|^{-\alpha}$ so that $R_\star^{-\frac{1}{\alpha}} = \min_{U_i \in \Phi_u} \|U_i\|$ is the shortest distance between the origin and set Φ_u . Thus, using $F_{R_\star}(r)$ in (5) helps find the CCDF of $R_\star^{-\frac{2}{\alpha}}$ as

$$F_{R_{\star}^{\frac{2}{\alpha}}}^{c}(y) = \exp\left(-\pi\lambda\mathbb{E}\left[\cos^{2}(\Theta)\right]y\right),$$
 (9)

which indicates that $R_{\star}^{-2/\alpha} \sim \exp(\pi \lambda \mathbb{E}[\cos^2(\Theta)])$ is an exponential RV with mean $1/\pi \lambda \mathbb{E}[\cos^2(\Theta)]$, and it is exactly the CCDF of the square of the shortest distance between the origin and a 2D homogeneous PPP of density $\lambda \mathbb{E}[\cos^2(\Theta)]$ [20], [21]. Namely, this observation manifests that the 3D point process Φ_u proposed in (2) can be equivalently viewed as a 2D homogeneous PPP of density $\lambda \mathbb{E}[\cos^2(\Theta)]$ as long as the elevation angle and the projection of each point in Φ_u are independent. Moreover, using (7) for this case yields $F_{R-2/\alpha}^c(y)$ given by

$$\begin{split} F_{R_{\star}^{\frac{2}{\alpha}}}^{c}(y) &= \exp\left[-\pi\lambda\Omega\left(y^{-\frac{\alpha}{2}}\right)\right] \\ &= \exp\left[-\pi\int_{0}^{y}\lambda F_{H}(\sqrt{z})\mathrm{d}z\right]. \end{split} \tag{10}$$

For this case, Φ_u can be viewed as a 2D non-homogeneous PPP of location-dependent density $\lambda F_H(\sqrt{z})$. Thus, we can conclude that Φ_u becomes a 2D non-homogeneous PPP whenever the elevation angle and the projection of each point in Φ_u are not independent (i.e., the APDL scenario). There is a simple example which demonstrates this scenario, that is, if all the points in Φ_u are positioned at the same altitude of \overline{h} , we know $\Theta_i = \tan^{-1}(\overline{h}/\|X_i\|)$ so that $F_{R_\star}^c(y) = \exp(-\pi \int_0^y \lambda \mathbb{1}(\overline{h} \leq \sqrt{z}) \mathrm{d}z)$ and Φ_u is a non-homogeneous PPP of density $\lambda \mathbb{1}(\overline{h} \leq \sqrt{z})$ for this example.

2) $W_i=1$: For this case, R_\star in (4) reduces to $R_\star=\max_{i:U_i\in\Phi_u}L_i\|U_i\|^{-\alpha}$ and thus $R_\star^{-\frac{1}{\alpha}}=\min_{i:U_i\in\Phi_u}\{L_i^{-\frac{1}{\alpha}}\|U_i\|\}$. Thus, the distribution of $R_\star^{-\frac{1}{\alpha}}$ can reflect how the LoS effect impacts the distribution of the shortest distance between the origin and set Φ_u . By considering W=1 in (5), we can obtain $F_{R_\star}^c$ (y) as shown in the following:

$$F_{R,\frac{2}{\alpha}}^{c}(y) = \exp\left(-\pi\lambda\omega y\right),\tag{11}$$

i.e., $R_{\star}^{-\frac{2}{\alpha}}\sim \exp(\pi\lambda\omega)$, which reveals that the following point set

set
$$\widetilde{\Phi}_u \triangleq \left\{ \widetilde{U}_i \in \mathbb{R}^2 \times \mathbb{R}_+ : \widetilde{U}_i = L_i^{-\frac{1}{\alpha}} U_i, L_i \in \{1,\ell\}, U_i \in \Phi_u \right\} \tag{12}$$

can be viewed as a thinning PPP from Φ_x with density $\lambda\omega$. When $\ell=0$, $R_\star^{-\frac{1}{\alpha}}$ is the shortest distance of the LoS link from the origin to set Φ_u and $F^c_{R_\star^{-\frac{2}{\alpha}}}(x)$ in (11) reduces to

 $e^{-\pi\lambda\mathbb{E}[\rho(\Theta)\cos^2(\Theta)]y}$. Therefore, in the APIL scenario the LoS points in Φ_u are equivalent to a 2D homogeneous PPP of density $\lambda\mathbb{E}[\cos^2(\Theta)\rho(\Theta)]$. Furthermore, for $F^c_{R_\star}^{\ \ 2}(y)$ in (7) with W=1, we can have

$$F_{R,\frac{2}{\alpha}}^{c}(y) = \exp\left[-\pi\lambda\Omega\left(y^{-\frac{\alpha}{2}}\right)\right],\tag{13}$$

where $\Omega(y^{-\alpha/2})$ is found from (8) for W=1 and it is given by

$$\Omega\left(y^{-\frac{\alpha}{2}}\right) = \mathbb{E}_{H}\left[\left(y\ell^{\frac{2}{\alpha}} - H^{2}\right)^{+} + \int_{\left(y\ell^{\frac{2}{\alpha}} - H^{2}\right)^{+}}^{\left(y-H^{2}\right)^{+}} \rho\left(\tan^{-1}\left(\frac{H}{\sqrt{z}}\right)\right) dz\right], \tag{14}$$

where $(x)^+ \triangleq \max\{0,x\}$. Hence, $\widetilde{\Phi}_u$ can be viewed as a 2D non-homogeneous PPP of density $\lambda \frac{\mathrm{d}\Omega(z)}{\mathrm{d}z}$ since $R_\star^{-\frac{1}{\alpha}}$ is the shortest distance from the origin to $\widetilde{\Phi}_u$. More specifically, if $\ell=0$ and H is equal to a constant $\overline{h}>0$, we further know $\Omega(y^{-\frac{\alpha}{2}})=\int_0^{(y-\overline{h}^2)^+}\rho(\tan^{-1}(\overline{h}/\sqrt{z}))\mathrm{d}z$, which reveals that the LoS points in Φ_u can be equivalently viewed as a 2D non-homogeneous PPP of density $\lambda\rho(\tan^{-1}(\overline{h}/\sqrt{z}))$ in the APDL scenario. Also, (14) implicitly indicates that $\Omega(y^{-\frac{\alpha}{2}})$ is significantly dependent upon the mean of H, especially when $y\ell^{\frac{2}{\alpha}}$ is small. Namely, in general $\Omega(y^{-\frac{\alpha}{2}})$ in (14) is insensitive to the different distributions of H that have the same mean. This point will be illustrated in Section IV-B.

These above observations learned from R_{\star} considerably help us understand some fundamental and intrinsic properties of Φ_u and they are very useful for the following analyses.

B. Laplace Transforms of the 3D Shot Signal Processes in Φ_u

Let the Laplace transform of a non-negative RV Z be defined as $\mathcal{L}_Z(s) \triangleq \mathbb{E}[\exp(-sZ)]$ for s>0. In this subsection, we would like to first study the Laplace transform of the following RV T_0 defined as

$$T_0 \triangleq \sum_{i:U_i \in \Phi_u} W_i L_i ||U_i||^{-\alpha}, \tag{15}$$

which is referred to as a (complete) 3D (Poisson) shot signal process since it is the sum of all the weighted signal measures in a 3D Poisson field of transmitting points [24]–[26]. Study the Laplace transform of T_0 gives rise to some useful results that can be employed to the following coverage analyses of a UAV-enabled cellular network in Section III as the proposed 3D point process Φ_u is applied to model the locations of UAVs hovering in the sky. Our findings for $\mathcal{L}_{T_0}(s)$ are summarized in the following theorem.

Theorem 2. Suppose the moment and the Laplace transform of W_i exist for all $i \in \mathbb{N}_+$. (i) If the APIL scenario is considered such that Θ_i and X_j are independent for all $i, j \in \mathbb{N}_+$, $\mathcal{L}_{T_0}(s)$ can be found as

$$\mathcal{L}_{T_0}(s) = \exp\left\{-\pi \lambda s^{\frac{2}{\alpha}} \mathbb{E}\left[W^{\frac{2}{\alpha}}\right] \Gamma\left(1 - \frac{2}{\alpha}\right) \omega\right\}, \quad (16)$$

where $\Gamma(z) \triangleq \int_0^\infty y^{z-1} e^{-y} dy$ for z > 0 is the Gamma function. (ii) On the other hand, if the APDL scenario is

considered such that $\Theta_k = \tan^{-1}(H_k/\|X_k\|)$ for all $k \in \mathbb{N}_+$, $\mathcal{L}_{T_0}(s)$ can be derived as

$$\mathcal{L}_{T_0}(s) = \exp\left(-\pi\lambda \int_0^\infty \mathcal{J}_W\left(sz^{-\frac{\alpha}{2}}, \tan^{-1}\left(\frac{H}{\sqrt{z}}\right)\right) dz\right),\tag{17}$$

where $\mathcal{J}_W(x,Y)$ for x,Y>0 is defined as

$$\mathcal{J}_{W}(x,Y) \triangleq \mathbb{E}_{Y} \left\{ \rho(Y) \left[1 - \mathcal{L}_{W} \left(x \cos^{\alpha}(Y) \right) \right] + \left[1 - \rho(Y) \right] \left[1 - \mathcal{L}_{W} \left(x \ell \cos^{\alpha}(Y) \right) \right] \right\}. \tag{18}$$

Proof: See Appendix B.

Note that (17) reduces to its closed-form version in (16) once the dependence between the elevation angle and the projection of each point in Φ_u does not exit. We can infer the distribution of T_0 from Theorem 2. Let $f_{T_0}(\cdot)$ denote the probability density function (PDF) of T_0 and it can be obtained by finding the inverse Laplace transform of T_0 . Namely, by letting $\mathcal{L}^{-1}\{g(s)\}(z)$ denote the inverse Laplace transform of function g(s), we can express the PDF of T_0 for the result in (16) as

$$f_{T_0}(z) = \mathcal{L}^{-1} \left\{ \exp \left[-\pi \lambda s^{\frac{2}{\alpha}} \mathbb{E} \left[W^{\frac{2}{\alpha}} \right] \Gamma \left(1 - \frac{2}{\alpha} \right) \omega \right] \right\} (z), \tag{19}$$

which cannot be further found in closed form if $\alpha \neq 4$, yet it can be evaluated by numerical techniques. For $\alpha = 4$, the closed-form expression of $f_{T_0}(z)$ can be found as [25] [27]

$$f_{T_0}(z) = \frac{\pi \mathbb{E}[\sqrt{W}] \lambda \omega}{2z^{\frac{3}{2}}} \exp\left(-\frac{\pi^3 (\mathbb{E}[\sqrt{W}] \lambda \omega)^2}{4z}\right), \quad (20)$$

which is essentially the PDF of a Lévy RV with location parameter zero and scale parameter $\pi^3(\mathbb{E}[\sqrt{W}]\lambda\omega)^2/2$. Similarly, the PDF of T_0 for the result in (17) can also be expressed as

$$f_{T_0}(z) = \mathcal{L}^{-1} \left\{ \exp\left(-\pi\lambda \int_0^\infty \mathcal{J}_W\left(sz^{-\frac{\alpha}{2}}, \tan^{-1}\left(\frac{H}{\sqrt{z}}\right)\right) \right. dz \right) \right\} (z), \tag{21}$$

which does not have a closed-form solution and can only be evaluated by numerical methods.

Next, let us define the Kth-truncated shot signal process in Φ_u as follows

$$T_K \triangleq \sum_{k=K+1}^{\infty} W_k L_k ||U_k||^{-\alpha}, \tag{22}$$

where U_k denotes the kth nearest point in Φ_u to the origin, W_k and L_k are non-negative RVs associating with U_k as already defined in (4). Since T_K in (22) does not contain the weighted signals emitted from the K points in set Φ_u , it is called the Kth-truncated shot signal process in Φ_u and it converges to T_0 as K goes to zero. The Laplace transforms of T_K in two different scenarios are found in the following theorem.

Theorem 3. Suppose the moment and the Laplace transform of W_k for all $k \in \mathbb{N}_+$ exist. If the APIL scenario is considered such that Θ_i is independent of $||X_j||$ for all $i, j \in \mathbb{N}_+$, the

Laplace transform of T_K defined in (22) for K>0 can be derived as

$$\mathcal{L}_{T_K}(s) = \mathbb{E}_{D_K} \left\{ \exp\left(-\pi\lambda D_K \mathbb{E}_{\Theta} \left[[1 - \rho(\Theta)] \times \mathcal{I}_W \left(s\ell \cos^{\alpha}(\Theta) D_K^{-\frac{\alpha}{2}}, \frac{2}{\alpha} \right) + \rho(\Theta) \times \mathcal{I}_W \left(s\cos^{\alpha}(\Theta) D_K^{-\frac{\alpha}{2}}, \frac{2}{\alpha} \right) + \right] \right) \right\}, \tag{23}$$

where $D_K \sim \text{Gamma}(K, \pi \lambda)$ is a Gamma RV with shape parameter K and rate parameter $\pi \lambda$, and $\mathcal{I}_W(u, v)$ for u, v > 0 is defined as

$$\mathcal{I}_{W}(u,v) \triangleq u^{v} \left\{ \Gamma(1-v) \mathbb{E}\left[W^{v}\right] - \int_{0}^{u^{-v}} \left[1 - \mathcal{L}_{W}\left(x^{-\frac{1}{v}}\right)\right] dx \right\}. \tag{24}$$

On the contrary, if the APDL scenario is considered such that $\Theta_i = \tan^{-1}(H_i/\|X_i\|)$, $\mathcal{L}_{T_K}(s)$ is found as

$$\mathcal{L}_{T_K}(s) = \mathbb{E}_{D_K} \left\{ \exp \left[-\pi \lambda \int_{D_K}^{\infty} \mathcal{J}_W \left(\frac{s}{z^{\frac{\alpha}{2}}}, \tan^{-1} \left(\frac{H}{\sqrt{z}} \right) \right) \right. \right.$$

$$\left. dz \right] \right\}.$$
(25)

Proof: See Appendix C.

Although the result in (25) is somewhat complicated due to considering the dependence between the elevation angle and the project of each point in Φ_u , it reduces to the result in (23) once the dependence no longer exists. In general, (23) cannot be further expressed as a closed-form outcome, yet it simply reduces to the following expression for a special case of $s = \zeta \sec^{\alpha}(\Theta)D_{K}^{\frac{\alpha}{2}}$ for any constant $\zeta > 0$:

$$\mathcal{L}_{T_K} \left(\zeta \sec^{\alpha}(\Theta) D_K^{\frac{\alpha}{2}} \right) = \left[1 + \mathbb{E} \left[\rho(\Theta) \right] \mathcal{I}_W \left(\zeta, \frac{2}{\alpha} \right) + \left(1 - \mathbb{E} \left[\rho(\Theta) \right] \right) \mathcal{I}_W \left(\zeta \ell, \frac{2}{\alpha} \right) \right]^{-K},$$
(26)

and we will find this result quite useful for the analyses in the following sections. In general, the PDF of T_K cannot be tractably derived by finding the inverse Laplace transforms of (23) and (25) thanks to their complicated forms. Nevertheless, we will see that Theorem 3 plays a pivotal role in the following coverage analyses of a UAV-enabled cellular network.

III. MODELING AND ANALYSIS OF A UAV-ENABLED CELLULAR NETWORK USING Φ_u

In this section, we employ the proposed 3D point process Φ_u in (2) to model the random locations of UAVs in a cellular network, as shown in Fig. 1. The salient feature of using Φ_u to model the 3D locations of the UAVs, as we will see, is not only to generally characterize the distribution of the UAVs hovering in the sky but also to properly and tractably analyze the performances of a UAV-enabled cellular network. Our focus in this section is on the study of the coverage performance of a UAV-enabled cellular network in

which a tier of UAVs are deployed in the sky that serve as *aerial* base stations in the network and the locations of the UAVs are modeled by Φ_u , that is, U_i in Φ_u denotes UAV i and its location in the network. Note that in this paper our focus is to study how to generally deploy a large-scale UAV-enabled cellular network and analyze its performances of a snapshot in time so that in general the proposed Φ_u cannot characterize the continuous-time mobility impacts of the UAVs on the network performances. Nonetheless, Φ_u still works for modeling the positions of all mobile UAVs whose trajectories are quiet different at any particular time point in that they can be properly assumed to be independent and thereby well approximated by Φ_u .

Suppose there is a typical user located at the origin and each user in the UAV-enabled cellular network associates with a UAV that provides it with the (averaged) strongest received signal power. Namely, the UAV associated with the typical user is given by

$$U_{\star} \triangleq \arg \max_{i:U_{i} \in \Phi_{u}} \mathbb{E} \left[PL_{i}G_{i} \|U_{i}\|^{-\alpha} |U_{i} \right]$$

$$= \arg \max_{i:U_{i} \in \Phi_{u}} \frac{P\mathbb{E}[G]L_{i}}{\|U_{i}\|^{\alpha}}$$

$$= \arg \max_{i:U_{i} \in \Phi_{u}} \frac{L_{i}}{\|U_{i}\|^{\alpha}}, \tag{27}$$

where P is the transmit power of each UAV, $G_i \sim \exp(1)$ denotes the fading channel gain between the typical user⁴ and U_i , $\alpha > 2$ denotes the path-loss exponent in this context, and L_i , as already defined in (4), is used to characterize the LoS and NLoS channel effects in the channel between U_i and the typical user. The second equality in (27) is due to considering the independence between G_i and U_i as well as conditioning on U_i , and the third equality is owing to removing constants P and $\mathbb{E}[G]$ does not affect the result of finding U_{\star} .

A. The SINR Model

Let I_0 be the aggregated interference power received by the typical user that does not include the signal power from U_{\star} so that it can be written as

$$I_0 \triangleq \sum_{i:U_i \in \Phi_u \setminus U_*} PG_i L_i ||U_i||^{-\alpha}. \tag{28}$$

All G_i 's are assumed to be i.i.d. and they are independent of all L_i 's and U_i 's. Note that each UAV is associated with at least one user so that the "void" UAV phenomenon is not modeled in I_0 [28] [29]. In addition, each UAV allocates different resource blocks (RBs) to different users associating with it, i.e., no users associating with the same UAV can share the same RB.

Each UAV is assumed to be equipped with N antennas whereas each user is equipped with a single antenna. According to (27) and (28), if each UAV is able to perform transmit

 4 The fading channel gain G_i is assumed to be an exponential RV with unit mean and not affected by the N transmit antennas of a UAV because each UAV broadcasts its user association signaling during the phase of user association and thereby it cannot do downlink transmit beamforming to any specific user.

beamforming to its user, the signal-to-interference plus noise power ratio (SINR) of the typical user can be defined as

$$\gamma_0 \triangleq \frac{PG_{\star}L_{\star}||U_{\star}||^{-\alpha}}{I_0 + \sigma_0},\tag{29}$$

where $G_{\star} \sim \text{Gamma}(N, 1)$ is the fading channel gain from U_{\star} to the typical user⁵, $L_{\star} \in \{1, \ell\}$ has the same distribution as L_i , and σ_0 denotes the thermal noise power from the environment. The downlink coverage (probability) of a user in the network can thus be defined as

$$p_{cov} \triangleq \mathbb{P}\left[\gamma_0 \ge \beta\right] = \mathbb{P}\left[\frac{PG_{\star}L_{\star}||U_{\star}||^{-\alpha}}{I_0 + \sigma_0} \ge \beta\right], \quad (30)$$

where $\beta > 0$ is the SINR threshold for successful decoding. In the following, we will analyze p_{cov} by considering whether the elevation angle and the projection of each UAV are independent or not. In the following two sections, we will employ the model of the UAV-enabled cellular network proposed in this section to analyze the coverage performances of the network in the APIL and APDL scenarios.

B. Downlink Coverage Analysis: The APIL Scenario

In this subsection, we would like to study the downlink coverage p_{cov} in (30) by considering the APIL scenario, i.e., elevation angle Θ_i and projection X_i of UAV U_i are independent for all $i \in \mathbb{N}_+$. The following proposition, which is developed by employing Theorem 3 to a first-truncated shot signal process in the 3D point process $\widetilde{\Phi}_u$ defined in (12), specifies the analytical result of p_{cov} in this scenario.

Proposition 1. If the APIL scenario is considered, the downlink coverage defined in (30) can be found as

$$p_{cov} = \frac{\mathrm{d}^{N-1}}{\mathrm{d}t^{N-1}} \mathbb{E} \left[\frac{t^{N-1}}{(N-1)!} \exp\left(-\frac{\sigma_0 D_{\star}^{\frac{\alpha}{2}}}{tP}\right) - \pi \lambda \omega D_{\star} \mathcal{I}_G \left(\frac{1}{t}, \frac{2}{\alpha}\right) \right] \Big|_{t=\frac{1}{2}},$$
(31)

where $D_{\star} \sim \exp(\pi \lambda \omega)$ and function $\mathcal{I}_G(u,v)$ is defined as

$$\mathcal{I}_G(u,v) \triangleq u^v \left(\frac{\pi v}{\sin(\pi v)} - \int_0^{u^{-v}} \frac{\mathrm{d}r}{1 + r^{\frac{1}{v}}} \right). \tag{32}$$

Proof: See Appendix D.

We adopt an exponential RV D_{\star} with mean $1/\pi\lambda\omega$ in (31) to make p_{cov} show in a neat form so as to clearly see how p_{cov} is impacted by D_{\star} and other network parameters. The physical meaning of D_{\star} is the square of the shortest distance between the typical user and set $\widetilde{\Phi}_u$, i.e., $D_{\star} \triangleq \|\widetilde{U}_{\star}\|^2 \stackrel{d}{=} L_{\star}^{-\frac{2}{\alpha}} \|U_{\star}\|^2$ where \widetilde{U}_{\star} is the nearest point in $\widetilde{\Phi}_u$ to the typical user and $\frac{d}{d}$

 $^5\mathrm{The}$ fading channel gain G_\star is assumed to be a Gamma RV with shape parameter N and rate parameter 1 (i.e., $G_\star \sim \mathrm{Gamma}(N,1)$) because UAV U_\star is serving the typical user so that it knows the channel state information (CSI) of the typical user and is thus able to do downlink transmit beamforming to the typical user. Hence, the mean of G_\star is $\mathbb{E}[G_\star]=N$. All the fading channel gains in I_0 can be shown to be i.i.d. exponential RVs with unit mean (i.e., $G_i \sim \exp(1)$) since all the interfering UAVs do not know the CSI from them to the typical user and are thus unable to do transmit beamforming to the typical user. For the detailed explanation about how to derive $G_\star \sim \mathrm{Gamma}(N,1)$ and $G_i \sim \exp(1)$, please refer to Appendix A in [30] or Section II-D in [31].

stands for the equivalence in distribution. In other words, p_{cov} is highly dependable upon the distribution of elevation angle Θ and ℓ for a given density λ because the distribution of D_{\star} is parameterized with $\lambda \omega$. To make this point much clear, we use Jensen's inequality to find a lower bound on p_{cov} in (31)

$$p_{cov} \ge \frac{1}{(N-1)!} \frac{\mathrm{d}^{N-1}}{\mathrm{d}t^{N-1}} \left\{ t^{N-1} \exp\left[-\frac{\sigma_0 \Gamma\left(1 + \frac{\alpha}{2}\right)}{tP(\pi \lambda \omega)^{\frac{\alpha}{2}}} - \mathcal{I}_G\left(\frac{1}{t}, \frac{2}{\alpha}\right)\right] \right\} \Big|_{t=\frac{1}{\alpha}},$$
(33)

which reduces to the following neat inequality for N=1:

$$p_{cov} \ge \exp\left[-\frac{\beta\sigma_0\Gamma\left(1+\frac{\alpha}{2}\right)}{P(\pi\lambda\omega)^{\frac{\alpha}{2}}} - \mathcal{I}_G\left(\beta,\frac{2}{\alpha}\right)\right].$$
 (34)

The inequalities in (33) and (34) apparently show that increasing $\lambda\omega$ improves p_{cov} . This is because users are able to associate with a nearer UAV and receive stronger power from the UAV when deploying UAVs more densely even though more interference is generated as well. Also, p_{cov} improves whenever $\lambda\omega$ can be maximized by optimizing the distribution of Θ . We will demonstrate some numerical results in Section IV to show how p_{cov} varies with different distribution cases of Θ . However, when the network is interference-limited (i.e., $\sigma_0=0$), p_{cov} in (31) significantly reduces to the following expression

$$p_{cov} = \frac{1}{(N-1)!} \frac{\mathrm{d}^{N-1}}{\mathrm{d}t^{N-1}} \left(\frac{t^{N-1}}{1 + \mathcal{I}_G\left(\frac{1}{t}, \frac{2}{\alpha}\right)} \right) \Big|_{t=\frac{1}{\beta}}$$

$$\stackrel{(N=1)}{=} \frac{1}{1 + \mathcal{I}_G(\beta, \frac{2}{\alpha})}, \tag{35}$$

and further reduces to a closed-form result as N=1, which is not impacted by $\lambda\omega$. Thus, we can draw a conclusion that the downlink coverage tends to be more sensitive to the distribution of the elevation angle and the density of the projections of the UAVs as the network tends to be more "noise-limited" (i.e., noise power dominates the SINR performance). Moreover, as N goes to infinity, p_{cov} in (31) increases up to the following limit

$$p_{cov,\infty} \triangleq \lim_{N \to \infty} p_{cov}$$

$$= \mathcal{L}^{-1} \left\{ \mathbb{E} \left[\frac{1}{s} \exp \left(-\frac{s\sigma_0 D_{\star}^{\frac{\alpha}{2}}}{P} - \pi \lambda \omega D_{\star} \right) \right] \right\} \left(\frac{1}{\beta} \right), \tag{36}$$

which is the upper limit of the downlink coverage for a user associating with a single UAV with a massive antenna array.

An effective method to significantly improve the coverage of users is to make users associate with multiple UAVs so that the UAVs can do coordinated multi-point (CoMP) joint transmission. The upper limit of the downlink coverage of a user associating with multiple UAVs can be achieved when all the UAVs are coordinated to jointly transmit to the user at the same time, which is referred as to the *cell-free downlink coverage*. Since perfectly coordinating and synchronizing all

the UAVs in a large-scale network to do *coherent* transmission is hardly possible in practice, *non-coherent joint transmission* is a feasible way for all the UAVs to jointly achieve the cell-free downlink coverage in that it has lower implementation complexity and does not require large backhaul capacity if compared with its coherent counterpart⁶. When all the UAVs perform non-coherent CoMP joint transmission to a user, the cell-free downlink coverage of the user can be defined as [32], [33]

$$p_{cov}^{cf} \triangleq \mathbb{P}\left[\frac{P\sum_{i:U_i \in \Phi_u} G_i L_i \|U_i\|^{-\alpha}}{\sigma_0} \ge \beta\right], \quad (37)$$

where $G_i \sim \text{Gamma}(N, 1)$ for all $i \in \mathbb{N}_+$ since all the UAVs can do transmit beamforming to the user. The explicit result of p_{cov}^{cf} can be found by using Theorem 2 and it is shown in the following proposition.

Proposition 2. If all the UAVs are deployed based on the APIL scenario and coordinated to do non-coherence joint transmission, the cell-free downlink coverage defined in (37) is derived as

$$p_{cov}^{cf} = 1 - \mathcal{L}^{-1} \left\{ \frac{1}{s} \exp\left[-\frac{\pi \lambda s^{\frac{2}{\alpha}} \omega}{(N-1)!} \Gamma\left(N + \frac{2}{\alpha}\right) \right] \right\} \left(\frac{\beta \sigma_0}{P} \right), \tag{38}$$

which reduces to the following closed-form result for $\alpha = 4$:

$$p_{cov}^{cf} = \operatorname{erf}\left(\frac{\pi^{\frac{3}{2}}\lambda\omega}{2(N-1)!}\sqrt{\frac{P}{\beta\sigma_0}}\Gamma\left(N+\frac{1}{2}\right)\right),\tag{39}$$

where $\operatorname{erf}(z) \triangleq \frac{2}{\sqrt{\pi}} \int_0^z e^{-t^2} dt$ is the error function for z > 0.

The cell-free downlink coverage in (37) can be interpreted as the maximum downlink coverage jointly achieved by all the UAVs with N antennas. When N goes to infinity, (38) approaches its upper limit given by

$$p_{cov,\infty}^{cf} \triangleq \lim_{N \to \infty} p_{cov}^{cf}$$

$$= 1 - \mathcal{L}^{-1} \left\{ \frac{1}{s} \exp \left[-\pi \lambda s^{\frac{2}{\alpha}} \omega \Gamma \left(1 - \frac{2}{\alpha} \right) \right] \right\} \left(\frac{\beta \sigma_0}{P} \right), \tag{40}$$

which reduces to the following closed-form results for $\alpha=4$:

$$p_{cov,\infty}^{cf} = \lim_{N \to \infty} p_{cov}^{cf} = \operatorname{erf}\left(\frac{\pi^{\frac{3}{2}}\lambda\omega}{2}\sqrt{\frac{P}{\beta\sigma_0}}\right).$$
 (41)

The cell-free downlink coverage in (40) and its closed-form special case in (41) are the fundamental limit of the downlink coverage achieved by all the UAVs that are equipped with a massive antenna array and perform non-coherent joint transmission and this fundamental limit is referred to as *the cell-free*

⁶Studying the fundamental limit of the downlink coverage of a UAVenabled cellular network is the main purpose in this paper. Accordingly, in the following analysis we merely analyze how much cell-free downlink coverage can be achieved when all the UAV adopt non-coherent joint transmission to serve one user. The cell-free downlink coverage problem of multiple users served by all the UAVs and its related practical issues are beyond the scope of this paper and they are left for our future study.

massive MIMO coverage of a UAV-enabled cellular network in the APIL scenario. To the best of our knowledge, they are firstly derived in this paper. Note that p_{cov}^{cf} is dominated by $\lambda \omega$ and P and increasing $\lambda \omega$ is more efficient to improve it than increasing P, and thereupon it is also significantly affected by the distribution of the elevation angle of the UAVs. Hence, optimizing the distribution of the elevation angle of each UAV may also considerably improve p_{cov}^{cf} , which will be numerically demonstrated in Section IV.

C. Downlink Coverage Analysis of a UAV-Enabled Network: The APDL Scenario

In the subsection, we turn our focus to the downlink coverage in the APDL scenario where the elevation angle and the projection of each UAV are dependent. For $\Theta_i = \tan^{-1}(H_i/\|X_i\|)$ for each UAV U_i , the following theorem summarizes the explicit expression of the downlink coverage in this scenario.

Proposition 3. If the APDL scenario is considered, the downlink coverage defined in (30) can be found as

$$p_{cov} = \frac{\mathrm{d}^{N-1}}{\mathrm{d}t^{N-1}} \mathbb{E}_{\widetilde{D}_{\star}} \left\{ \frac{t^{N-1}}{(N-1)!} \exp\left[-\frac{\sigma_0 \widetilde{D}_{\star}^{\frac{\alpha}{2}}}{Pt} - \pi \lambda \right] \times \widetilde{D}_{\star} \widetilde{\mathcal{I}}_G \left(\frac{1}{t}, \frac{2}{\alpha}, \widetilde{D}_{\star} \right) \right] \right\} \Big|_{t=\frac{1}{\beta}}, \tag{42}$$

where \widetilde{D}_{\star} is a non-negative RV with the following PDF

$$f_{\widetilde{D}_{\star}}(y) = \pi \lambda \Omega' \left(y^{-\frac{\alpha}{2}} \right) e^{-\pi \lambda \Omega \left(y^{-\frac{\alpha}{2}} \right)} \tag{43}$$

with $\Omega\left(y^{-\frac{\alpha}{2}}\right)$ is defined in (14) for the APDL scenario, $\Omega'\left(y^{-\frac{\alpha}{2}}\right) \triangleq \frac{\mathrm{d}\Omega\left(y^{-\frac{\alpha}{2}}\right)}{\mathrm{d}y}$, and $\widetilde{\mathcal{I}}_G(u,v,r)$ for u,v,r>0 is defined as

$$\widetilde{\mathcal{I}}_{G}(u, v, r) \triangleq \int_{1}^{\infty} \Omega' \left(\frac{r}{y^{v}}\right) \left(\frac{u}{y^{\frac{1}{v}} + u}\right) dy.$$
 (44)

Proof: See Appendix F.

Note that the physical meaning of \widetilde{D}_{\star} is the square of the short distance from the typical user to set $\widetilde{\Phi}_u$ in (12) in the APDL scenario and p_{cov} in (42) becomes p_{cov} in (31) as \widetilde{D}_{\star} in (42) reduces to D_{\star} in (31) (i.e., $\Omega(z)$ reduces to ωz). Applying the Jensen inequality on \widetilde{D}_{\star} in (42) gives rise to the following lower bound on p_{cov} in (42):

$$p_{cov} \ge \frac{\mathrm{d}^{N-1}}{\mathrm{d}t^{N-1}} \left\{ \frac{t^{N-1}}{(N-1)!} \exp\left[-\frac{\sigma_0 \mathbb{E}\left[\widetilde{D}_{\star}^{\frac{\alpha}{2}}\right]}{Pt} - \pi\lambda \right] \times \mathbb{E}[\widetilde{D}_{\star}]\widetilde{\mathcal{I}}_G\left(\frac{1}{t}, \frac{2}{\alpha}\right) \right\} \right\}_{t=\frac{1}{B}}$$
(45)

and for the interference-limited situation it reduces to

$$p_{cov} \ge \frac{\mathrm{d}^{N-1}}{\mathrm{d}t^{N-1}} \left\{ \frac{t^{N-1}}{(N-1)!} \exp\left[-\pi \lambda \mathbb{E}\left[\widetilde{D}_{\star}\right] \times \widetilde{\mathcal{I}}_{G}\left(\frac{1}{t}, \frac{2}{\alpha}\right)\right] \right\} \bigg|_{t=\frac{1}{B}}.$$
 (46)

According to the PDF of \widetilde{D}_{\star} in (43), we know $\mathbb{E}[\Omega(\widetilde{D}_{\star}^{-\frac{\alpha}{2}})] = \frac{1}{\pi\lambda}$ so that $\Omega(\mathbb{E}[\widetilde{D}_{\star}^{-\frac{\alpha}{2}}]) \leq \frac{1}{\pi\lambda}$ or $\Omega(\mathbb{E}[\widetilde{D}_{\star}^{-\frac{\alpha}{2}}]) \geq \frac{1}{\pi\lambda}$ depending

on the convexity of $\Omega(\cdot)$. In other words, $\lambda \mathbb{E}[\widetilde{D}_{\star}^{\frac{\alpha}{2}}]$ is still pertaining to λ and $\Omega(y^{-\frac{\alpha}{2}})$ so that the UAV density impacts the downlink coverage no matter whether or not the network is interference-limited, which is quite different from p_{cov} in (31). Therefore, properly deploying UAVs depending on the distribution of the altitude H of the UAVs is able to reduce $\lambda\Omega(y^{-\frac{\alpha}{2}})$ so as to improve the downlink coverage in the APDL scenario. For example, if each user associates with its nearest UAV with altitude $H \stackrel{d}{=} D_{\star}$ (i.e., $L_i = 1$ and $H \sim \exp(\pi \lambda)$ for all $i \in \mathbb{N}_+$, $\Omega(y^{-\frac{\alpha}{2}}) = F_H(y) =$ $1 - \exp(-\pi \lambda y)$ and $\Omega'(y^{-\frac{\alpha}{2}}) = f_H(y) = \pi \lambda \exp(-\pi \lambda y)$ based on the discussions in Section II-A. Thus, $\mathbb{E}\left|\widetilde{D}_{\star}^{\frac{\alpha}{2}}\right|$ and $\lambda \mathbb{E}[D_{\star}]$ decrease as λ increases such that p_{cov} always improves as more UAVs are deployed in this example. In addition, p_{cov} in (42) increases to its upper limit as the number of antennas equipped at each UAV goes to infinity, which can be shown by using the technique of inverse Laplace transform as used in (36).

Next, we would like to study how much the downlink coverage can be achieved when all the UAVs can perform the aforementioned non-coherent joint transmission in the previous subsection, i.e., the cell-free downlink coverage defined in (37) for the APDL scenario. The following proposition shows its explicit result.

Proposition 4. If all the UAVs are deployed based on the APDL scenario and coordinated to do non-coherence joint transmission, the cell-free downlink coverage in (37) can be derived as

$$p_{cov}^{ef} = 1 - \mathcal{L}^{-1} \left\{ \frac{1}{s} \exp\left[-\pi \lambda \int_{0}^{\infty} \mathcal{J}_{G} \left(sz^{-\frac{\alpha}{2}}, \right) \right] \right\} \left(\frac{\beta \sigma_{0}}{P} \right), \tag{47}$$

where $\mathcal{J}_G(x,Y)$ is

$$\mathcal{J}_{G}(x,Y) = 1 - \mathbb{E}_{Y} \left\{ \rho(Y) \left(1 + \frac{x \cos^{\alpha}(Y)}{N} \right)^{-N} + \left[1 - \rho(Y) \right] \left(1 + \frac{x \cos^{\alpha}(Y)\ell}{N} \right)^{-N} \right\}. \tag{48}$$

Also, as $N \to \infty$, we have

$$\lim_{N \to \infty} \mathcal{J}_G(x, Y) = 1 - \mathbb{E}_Y \left\{ \rho(Y) e^{-x \cos^{\alpha}(Y)} + [1 - \rho(Y)] \times e^{-x\ell \cos^{\alpha}(Y)} \right\}. \tag{49}$$

Proof: The proof is omitted since it is similar to the proof of Proposition 2.

Note that the cell-free massive MIMO coverage $p_{cov,\infty}^{cf}$ can be readily found by substituting (49) into (47) and it is the fundamental limit of the downlink coverage achieved in a UAV-enabled cellular networks for the APDL scenario. In general, the closed form of p_{cov} (47) cannot be derived, yet it does exist in some special cases. For example, when the altitudes of the UAVs are controlled such that they are proportional to their projection distance (i.e., $H_i = h_0 \|X_i\|$

Transmit Power (mW) P	50
Density of set Φ_x (points (UAVs)/m ²) λ_x	$1.0 \times 10^{-7} \sim 1.0 \times 10^{-5}$ (or see figures)
Number of Antennas N	$1, 4, 8, \infty$ (or see figures)
Noise Power (dBm) σ_0	-92.5
Path-loss Exponent α	2.75
Parameters (c_1, c_2) in (3) for Suburban	(24.5811, 39.5971)
NLoS Channel Attenuation Factor ℓ	0.25
SINR Threshold (dB) β	−10 (or see figures)

TABLE I NETWORK PARAMETERS FOR SIMULATION [22]

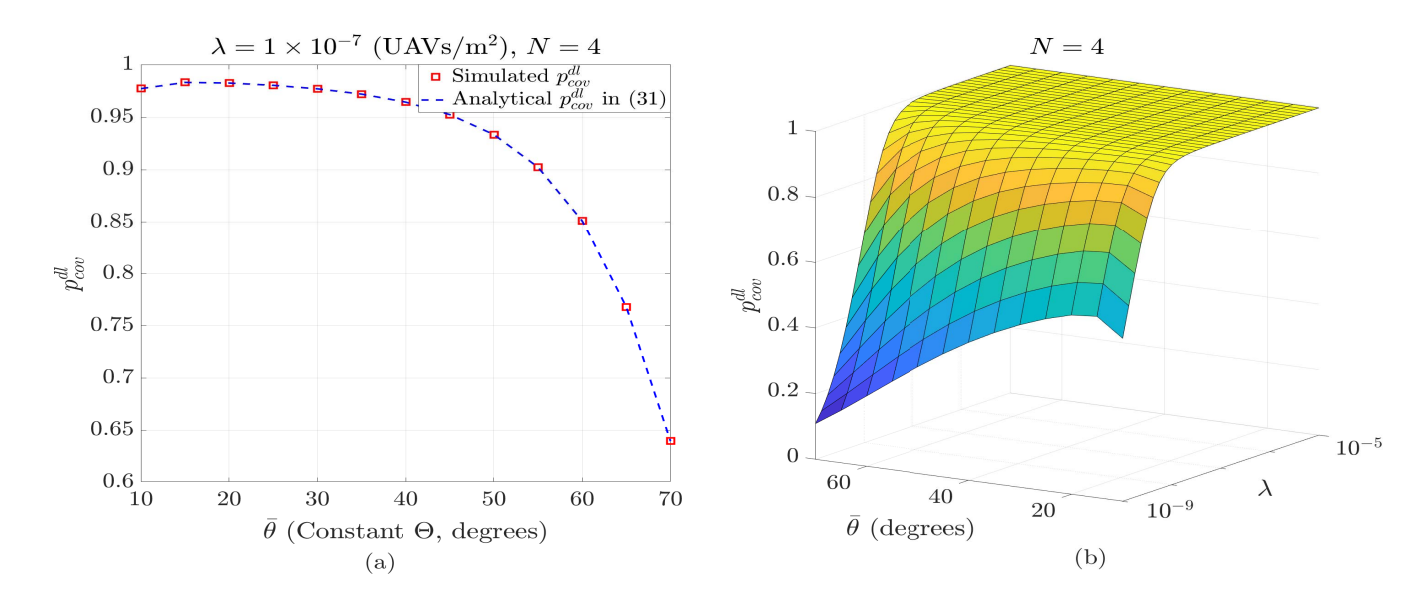


Fig. 2. Simulation results of p_{cov}^{dl} for the APIL scenario when N=4 and the elevation angle of each UAV is a constant $\overline{\theta}$ with respect to the origin (i.e., $\tan(\Theta) \sim \operatorname{Gamma}(a,a/\tan(\overline{\theta}))$ as $a\to\infty$): (a) The 2D simulation results of p_{cov}^{dl} versus elevation angle $\overline{\theta}$ for $\lambda=1\times 10^{-7}$ (UAV /m²), (b) The 3D simulation results of p_{cov}^{dl} versus density λ and elevation angel $\overline{\theta}$.

for some $h_0 > 0$ and all $i \in \mathbb{N}_+$), $\alpha = 4$ and $\ell = 1$, p_{cov}^{cf} in (47) reduces to the following closed-form expression

$$p_{cov}^{cf} = \operatorname{erf}\left(\frac{\pi\lambda}{2}\sqrt{\frac{P}{\beta\sigma_0}}\int_0^\infty \mathcal{J}_G\left(\frac{1}{z^2}, \tan^{-1}(h_0)\right) dz\right), \tag{50}$$

where $\mathcal{J}_G(z^{-2}, \tan^{-1}(h_0)) = 1 - \rho(\tan^{-1}(h_0))(1 + \cos^4(\tan^{-1}(h_0))/z^2N)^{-N}$. Also note that all the analytical outcomes in this section are valid as long as α is greater than two, which works for most practical 3D path-loss channel models. In the following section, we will present some numerical results to verify the above analytical findings of the downlink coverage.

IV. NUMERICAL RESULTS AND DISCUSSIONS

In this section, we will provide some numerical results to verify the previous analytical results of the downlink coverage. The numerical results of the APIL scenario will be presented and discussed first and those of the APDL will be shown and discussed afterwards. Finally, the numerical results of the downlink cell-free coverages will be presented. The network parameters adopted for simulation are shown in Table I and they are chosen from the real statistical data provided in [22]. Other simulation parameters needed for the APIL and APDL

scenarios will be specified in the following two subsections, respectively.

A. Simulation Results for the APIL Scenario

In this subsection, we present the simulation results of the downlink coverage for the APIL scenario. Specifically, we consider the tangent of the elevation angle of a UAV is a Gamma RV with shape parameter a and rate parameter b (i.e., $tan(\Theta) \sim Gamma(a, b)$ because using such a Gamma RV to model $tan(\Theta)$ is able to generally characterize different distributions by setting different values of a and b so that appropriately adjusting a and b can make Θ reasonably distribute between 0 and $\frac{\pi}{2}$. For example, $\tan(\Theta)$ becomes deterministic and equal to $tan(\overline{\theta})$ such that Θ is equal to constant $\overline{\theta}$ if $b = a/\tan(\overline{\theta})$ and $a \to \infty$ and it becomes an exponential RV with rate parameter 1/b if a = 1. Figures 2 and 3 show the simulation results of the downlink coverage p_{cov}^{dl} when $\tan(\Theta)$ is a constant and a Gamma RV, respectively. As we can see, the simulation results of p_{cov}^{dl} in Figs. 2(a) and 3(a) do not differ much when $\bar{\theta} < 45^{\circ}$, which reveals that in general p_{cov}^{dl} is insensitive to the distribution of Θ when the mean of Θ is not very large. In fact, this phenomenon can be inferred from (31) in that p_{cov}^{dl} is affected by the distribution of Θ through ω in (6) that is insensitive to the distribution of Θ

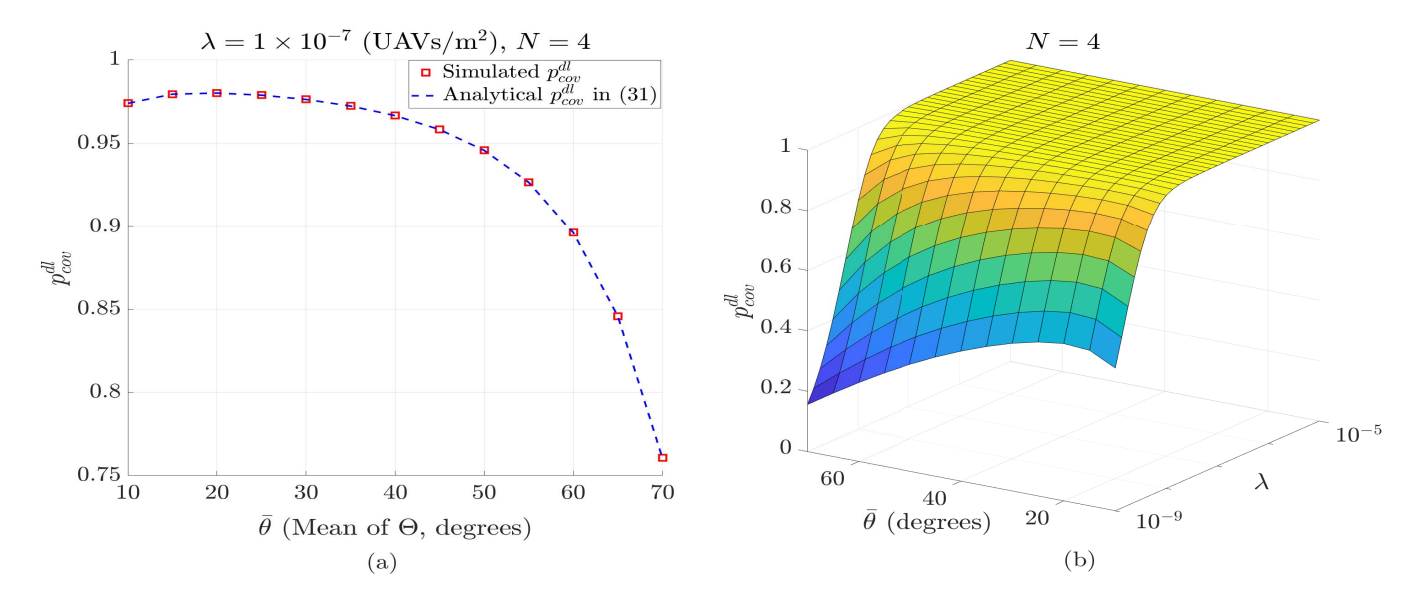


Fig. 3. Simulation results of p_{cov}^{dl} for the APIL scenario when N=4 and the elevation angle of each UAV is a Gamma RV with shape parameter a and rate parameter $a/\tan(\overline{\theta})$, i.e., $\tan(\Theta)\sim \mathrm{Gamma}(a,a/\tan(\overline{\theta}))$: (a) The 2D simulation results of p_{cov}^{dl} versus elevation angle Θ for $\lambda=1\times 10^{-7}$ (UAV/m²), (b) The 3D simulation results of p_{cov}^{dl} versus density λ and mean of elevation angel $\overline{\theta}$.

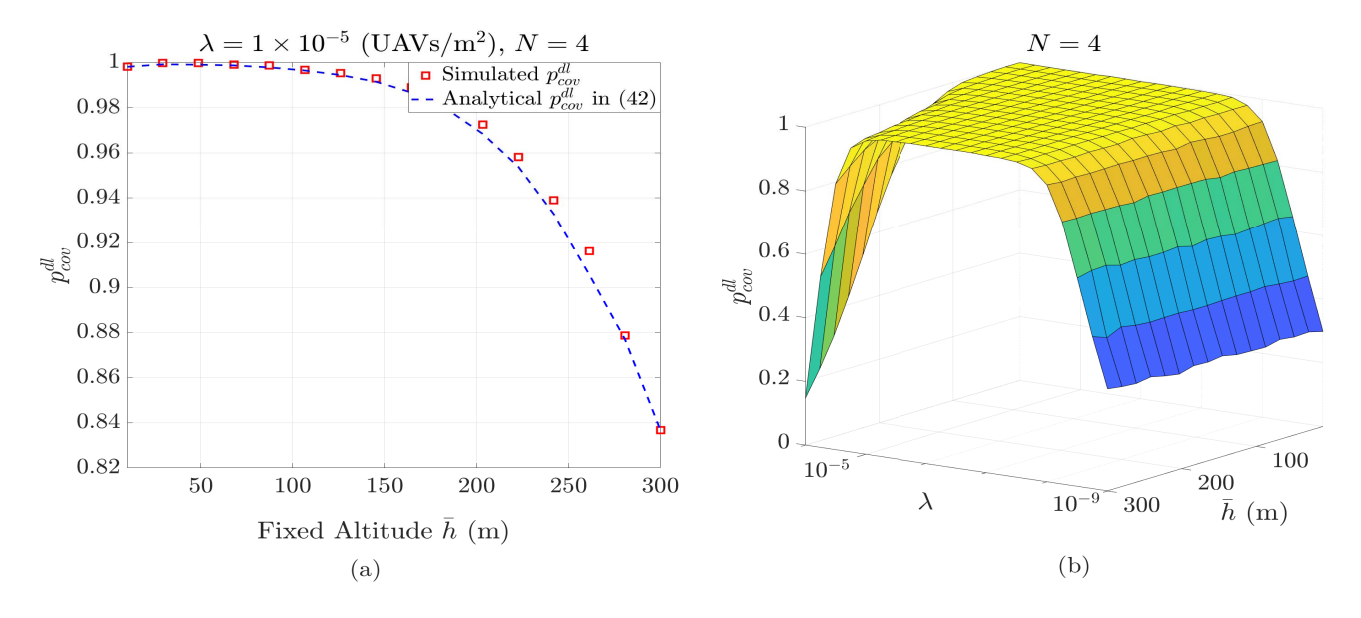


Fig. 4. Simulation results of p^{dl}_{cov} for the APDL scenario when N=4 and the altitude of each UAV is a constant \overline{h} (i.e., $H=\overline{h}$): (a) The 2D simulation results of p^{dl}_{cov} versus altitude \overline{h} for $\lambda=1\times 10^{-5}$ (UAV/m²), (b) The 3D simulation results of p^{dl}_{cov} versus density λ and the mean of altitude \overline{h} .

when the mean of Θ is not large. Realizing this phenomenon is quite useful since we can quickly and accurately calculate p_{cov}^{dl} using the mean of the elevation angle of UAVs in (31) without knowing the real distribution of Θ , which is in general not easy to find in practice.

Figures 2(a) and 3(a) validate the correctness and accuracy of the expression in (31) since the curve of the analytical result of p_{cov}^{dl} in (31) completely coincides with the curve of the simulated result of p_{cov}^{dl} . Moreover, there exists an optimal value of the mean of Θ about 20° for $\lambda=1\times10^{-7}$ (UAVs/m²), which maximizes p_{cov}^{dl} . Note that p_{cov}^{dl} decreases as the mean of Θ increases over 20° since the downlink SINR is now dominated by the interference in this situation even though the

received signal power also increases. The 3D plots in Fig. 2(b) and Fig. 3(b) further show how p_{cov}^{dl} varies with the mean of Θ and density λ . Generally speaking, the optimal value of the mean of Θ that maximizes p_{cov}^{dl} changes with density λ and p_{cov}^{dl} converges up to a constant as λ goes to infinity, i.e., p_{cov}^{dl} barely depends on λ as the network is dense and interference-limited, which is already shown in (35).

B. Simulation Results for the APDL Scenario

In this subsection, we specifically consider two distributions of the altitude of a UAV: one is *deterministic* (fixed) altitude and the other is *uniformly distributed* altitude. We would like to validate whether or not the analytical expression of p_{cov}^{dl}

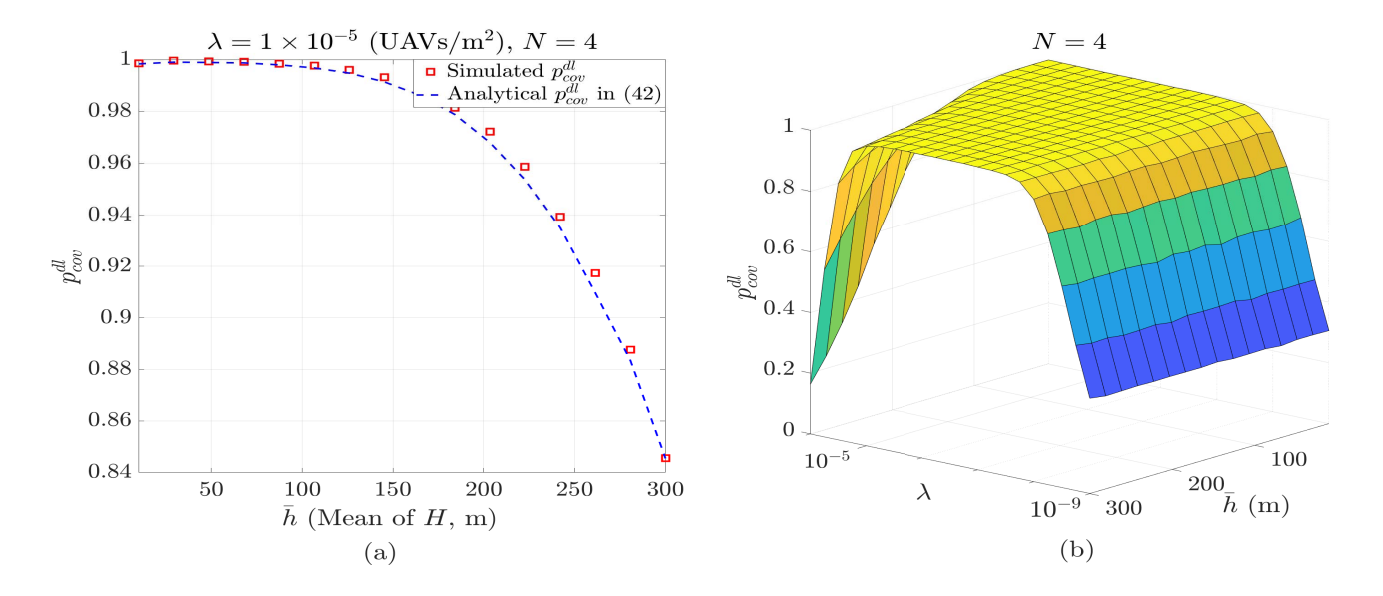


Fig. 5. Simulation results of p_{cov}^{cl} for the APDL scenario when N=4 and the altitude of each UAV is a uniformly distributed RV with mean \overline{h} (i.e., $H \sim \text{Uni}[\overline{h}-a,\overline{h}+a]$ for a>0): (a) The 2D simulation results of p_{cov}^{dl} versus altitude Θ for $\lambda=1\times 10^{-5}$ (UAV/m²), (b) The 3D simulation results of p_{cov}^{dl} versus density λ for $H \sim \text{Uni}[\overline{h}-5,\overline{h}+5]$.

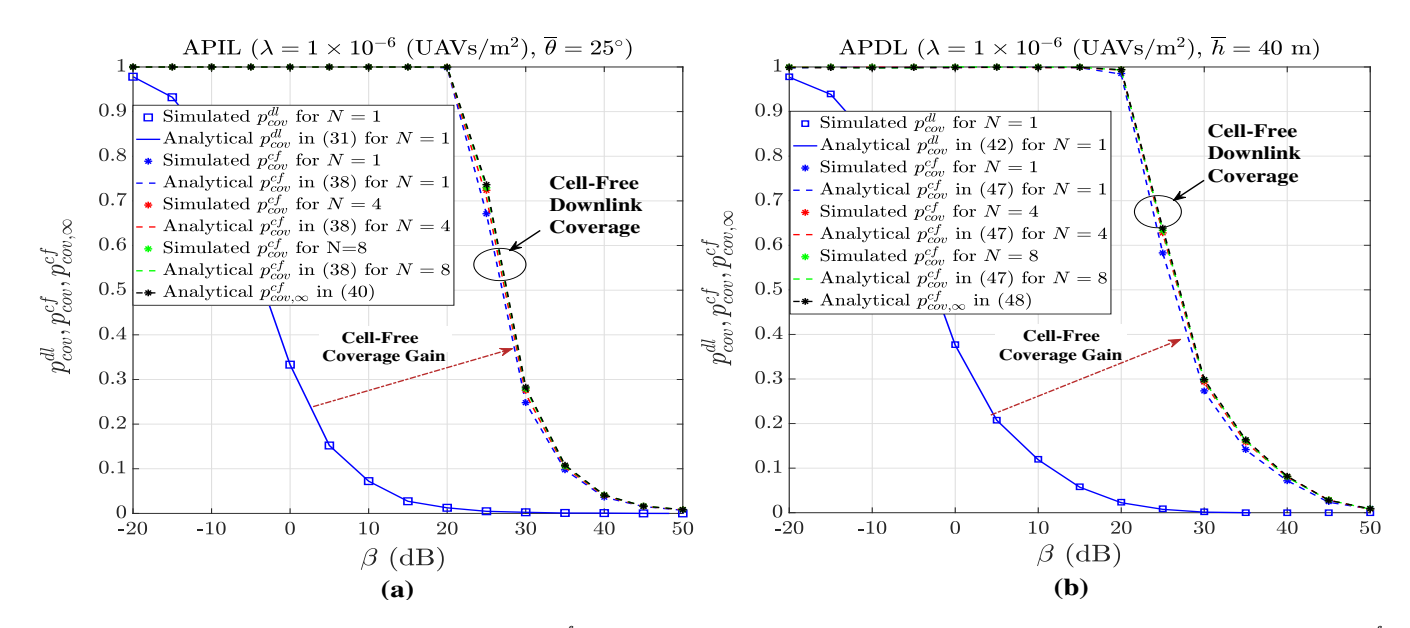


Fig. 6. Simulation results of cell-free downlink coverage p_{cov}^{cf} for $\lambda=1\times 10^{-6}$ (UAV/m²) and $N=1,2,4,8,\infty$: (a) The simulation results of p_{cov}^{cf} versus SINR threshold β for the APIL scenario and the elevation angle of each UAV is a constant equal to $\overline{\theta}=5^{\circ}$, (b) The simulation results of p_{cov}^{cf} versus SINR threshold β for the APDL scenario and the altitude of each UAV is a constant equal to $\overline{h}=40$ m.

in (42) is correct and illustrate how p_{cov}^{dl} varies with the two different distribution cases of the altitude of a UAV. When N=4, the simulation results of p_{cov}^{dl} for the distribution case of fixed altitude and the distribution case of uniformly distributed altitude are shown in Figs. 4 and 5, respectively. We see that the simulated results perfectly coincide with the analytical results of p_{cov}^{dl} obtained from (42) for $\lambda=1\times10^{-5}$ (UAVs/m²) in Figs. 4(a) and 5(a) so that the correctness of the expression in (42) is validated. The simulation results in Figs. 4(a) and 5(a) are very close so that in general p_{cov}^{dl} is insensitive to the different distributions of H that have the same mean and thus p_{cov}^{dl} can still be approximately calculated

by (42) with the mean of H even when the real distribution H is not known. Moreover, these two subplots both show that positioning UAVs too high significantly reduces p_{cov}^{dl} thanks to LoS interference. It is noteworthy that p_{cov}^{dl} degradation caused by LoS interference becomes apparent as λ is high, which can be observed from Figs. 4(b) and 5(b), yet p_{cov}^{dl} does not change much with the mean of H due to low interference when λ is small.

C. Simulation Results for Cell-Free Downlink Coverage

This subsection validates the analytical outcomes of the cell-free downlink coverage p_{cov}^{cf} for the APIL and APDL

scenarios. According to Fig. 6 that shows the numerical results of p_{cov}^{cf} , we can observe a few interesting and important phenomena. First, the analytical results of the downlink cellfree coverages in both of the subplots perfectly coincide with their corresponding simulated results, which validates the correctness of the expressions in (38), (40), (42), (47), (48), and (49). Second, the downlink cell-free coverages for different numbers of antennas are almost identical and this reveals that UAVs do not need to install multiple antennas to improve their coverage in the cell-free scenario so that UAVs can become lighter so as to save more power when flying. Third, the downlink cell-free coverage p_{cov}^{cf} significantly outperforms the downlink coverage p_{cov}^{dl} , as can be seen in the figure. For example, p_{cov}^{cf} for the APDL scenario and $\beta = 0$ dB is able to achieve 100%, yet p_{cov}^{dl} for the APDL scenario and $\beta = 0$ dB is only about 12%.

V. CONCLUSIONS

In the past decade, using 2D PPPs to model large-scale cellular networks had given rise to a great success in tractably analyzing the generic performance metrics of cellular networks. Nevertheless, straightforwardly employing a 3D PPP to deploy UAVs in a cellular network not only poses an unrealistic constraint on the path-loss exponent of 3D pathloss channel models, but also ignores a spatial deployment limitation in a cellular network, that is, in principle UAVs are low-altitude platforms that cannot be deployed in infinitely large 3D space modeled by a 3D PPP. Thus, there lack good 3D models with analytical tractability to deploy UAVs serving as aerial base stations in a large-scale cellular network. To tackle this issue, this paper proposes a 3D point process whose projections consist of a 2D homogeneous PPP and altitudes are the marks of the 2D homogeneous PPP. The fundamental properties of the proposed 3D point process are studied for the APIL and APDL scenarios and they pave a tractable way to analyze the downlink coverage of a UAV-enabled cellular network modeled by the proposed 3D point process. The downlink coverages for the APIL and APDL scenarios are explicitly derived and their closed-form expressions are also found for a special channel condition. In addition, cell-free downlink coverages and their upper limits are also derived when all the UAVs in the network can do non-coherence joint transmission.

APPENDIX

PROOFS OF THEOREMS AND PROPOSITIONS

A. Proof of Theorem 1

(i) Consider the APIL scenario so that X_i and Θ_j are independent for all $i, j \in \mathbb{N}_+$. Since $||U_i|| = ||X_i|| \sec(\Theta_i)$, the CDF of R_\star defined in (4) can be written as

$$\begin{split} F_{R_{\star}}(r) &= \mathbb{P}\left[\max_{i:U_{i} \in \Phi_{u}} \left\{\frac{W_{i}L_{i}}{[\|X_{i}\| \sec(\Theta_{i})]^{\alpha}}\right\} \leq r\right] \\ &\stackrel{(a)}{=} \mathbb{E}\left\{\prod_{i:U_{i} \in \Phi_{u}} \mathbb{P}\left[\frac{W_{i}L_{i}}{[\|X_{i}\| \sec(\Theta_{i})]^{\alpha}} \leq r\right]\right\} \end{split}$$

$$\stackrel{(b)}{=} \exp\left(-2\pi\lambda \int_0^\infty \mathbb{P}\left[\frac{WL}{[x\sec(\Theta)]^\alpha} \ge r\right] x \mathrm{d}x\right), \quad (A.1)$$

where (a) follows from the fact that all $W_iL_i[\|X_i\|\sec(\Theta_i)]^{-\alpha}$'s are independent and (b) is obtained by first considering the independence between all RVs W_i , L_i , $\|X_i\|$, and Θ_i for all $i \in \mathbb{N}_+$ and then applying the probability generation functional (PGFL) of a homogeneous PPP to Φ_x ⁷. According to (3), $\mathbb{P}[WL[x\sec(\Theta)]^{-\alpha} \geq r|\Theta]$ can be further expressed as

$$\mathbb{P}\left[\frac{WL}{[x\sec(\Theta)]^{\alpha}} \ge r \middle| \Theta\right] = \mathbb{P}\left[\left(\frac{W}{r}\right)^{\frac{1}{\alpha}}\cos(\Theta) \ge x \middle| \Theta\right] \rho\left(\Theta\right) + \mathbb{P}\left[\left(\frac{\ell W}{r}\right)^{\frac{1}{\alpha}}\cos(\Theta) \ge x \middle| \Theta\right] \times [1 - \rho\left(\Theta\right)].$$

Therefore, we can have the following:

$$\begin{split} &2\int_{0}^{\infty} \mathbb{P}\left[\frac{WL}{[x\sec(\Theta)]^{\alpha}} \geq r \middle| \Theta \right] x \mathrm{d}x \\ &= \rho(\Theta) \int_{0}^{\infty} \mathbb{P}\left[\left(\frac{W}{r}\right)^{\frac{1}{\alpha}} \cos(\Theta) \geq x \middle| \Theta \right] \mathrm{d}x^{2} + [1 - \rho(\Theta)] \\ &\times \int_{0}^{\infty} \mathbb{P}\left[\left(\frac{\ell W}{r}\right)^{\frac{1}{\alpha}} \cos(\Theta) \geq x \middle| \Theta \right] \mathrm{d}x^{2} \\ &= \cos^{2}(\Theta) \left[\rho(\Theta) + [1 - \rho(\Theta)]\ell^{\frac{2}{\alpha}}\right] \mathbb{E}\left[W^{\frac{2}{\alpha}}\right] r^{-\frac{2}{\alpha}} \end{split}$$

since $\int_0^\infty \mathbb{P}[Z \ge z] \mathrm{d}z = \mathbb{E}[Z]$ for a non-negative RV Z. This gives rise to the following result:

$$\begin{split} &2\int_{0}^{\infty} \mathbb{P}\left[\frac{WL}{[x\sec(\Theta)]^{\alpha}} \geq r\right] x \mathrm{d}x = \mathbb{E}\left[W^{\frac{2}{\alpha}}\right] r^{-\frac{2}{\alpha}} \\ &\times \mathbb{E}\left\{\cos^{2}(\Theta)\left[\rho(\Theta)\left(1-\ell^{\frac{2}{\alpha}}\right) + \ell^{\frac{2}{\alpha}}\right]\right\}, \end{split}$$

and then substituting this identity into (A.1) yields the expression in (5).

(ii) Consider the APDL scenario and we know $\Theta_i = \tan^{-1}(H_i/\|X_i\|)$ for $H_i > 0$. Since we know $\sec^2(\Theta_i) = 1 + H_i^2/\|X_i\|^2$ and $\Theta = \tan^{-1}(H/x)$, $\mathbb{P}[WL[x\sec(\Theta)]^{-\alpha} \geq r]$ in (A.1) for a given H can be rewritten as

$$\begin{split} & \mathbb{P}\left[\frac{WL}{x^{\alpha}(1+H^{2}/x^{2})^{\frac{\alpha}{2}}} \geq r \bigg| H\right] = \mathbb{P}\left[W \geq r(x^{2}+H^{2})^{\frac{\alpha}{2}}|H\right] \\ & \times \rho\left(\Theta\right) + \left[1-\rho\left(\Theta\right)\right] \mathbb{P}\left[W \geq \frac{r}{\ell}(x^{2}+H^{2})^{\frac{\alpha}{2}}|H\right] = \rho\left(\Theta\right) \\ & \times \mathbb{P}\left[W \geq rx^{\alpha}\sec^{\alpha}(\Theta)|H\right] + \left[1-\rho(\Theta)\right] \\ & \times \mathbb{P}\left[W \geq \frac{r}{\ell}x^{\alpha}\sec^{\alpha}(\Theta)|H\right]. \end{split}$$

Substituting this identity into (A.1) and replacing x^2 with z yield the expression in (7).

⁷Note that the subscript i in (a) is dropped in (b) for notation simplification and such a subscript dropping is used throughout this paper whenever there is no notation ambiguity.

B. Proof of Theorem 2

First, consider the APIL scenario in which the elevation angle and projection of point U_i are independent. Since the projections of all the points in Φ_u is a 2D homogeneous PPP of density λ and $\|U_i\| = \|X_i\| \sec(\Theta_i)$, the Laplace transform, $\mathcal{L}_{T_0}(s) = \mathbb{E}[\exp(-sT_0)]$, can be found as follows:

$$\mathbb{E}\left[e^{-sT_{0}}\right] = \mathbb{E}\left[\prod_{i:U_{i}\in\Phi_{u}}\exp\left(-\frac{sW_{i}L_{i}}{\|U_{i}\|^{\alpha}}\right)\right]$$

$$= \mathbb{E}_{\Phi_{u}}\left\{\prod_{i:X_{k}\in\Phi_{x}}\mathbb{E}_{WL}\left[\exp\left(-\frac{sW_{i}L_{i}}{(\|X_{i}\|\sec(\Theta_{i}))^{\alpha}}\right)\right]\right\}$$

$$\stackrel{(a)}{=}\exp\left(-\pi\lambda\int_{0}^{\infty}\left\{1 - \mathbb{E}\left[e^{-sWL(x\sec(\Theta))^{-\alpha}}\right]\right\}\mathrm{d}x^{2}\right)$$

$$\stackrel{(b)}{=}\exp\left(-\pi\lambda\int_{0}^{\infty}\mathbb{P}\left[Y \leq sWL\cos^{\alpha}(\Theta)z^{-\frac{\alpha}{2}}\right]\mathrm{d}z\right)$$

$$=\exp\left(-\pi\lambda\int_{0}^{\infty}\mathbb{P}\left[z \leq \cos^{2}(\Theta)\left(\frac{sWL}{Y}\right)^{\frac{2}{\alpha}}\right]\mathrm{d}z\right),$$
(A.3)

where (a) is obtained by applying the PGFL of a homogeneous PPP to Φ_x and (b) is obtained by first replacing x^2 with z and then rewriting the result in the integral by using $Y \sim \exp(1)$). In addition, we can have

$$\begin{split} & \int_0^\infty \mathbb{P}\left[z \le \cos^2(\Theta) \left(\frac{sWL}{Y}\right)^{\frac{2}{\alpha}}\right] \mathrm{d}z = s^{\frac{2}{\alpha}} \mathbb{E}\left[W^{\frac{2}{\alpha}}\right] \mathbb{E}\left[Y^{-\frac{2}{\alpha}}\right] \\ \mathbb{E}\left[\cos^2(\Theta)L^{\frac{2}{\alpha}}\right] & \stackrel{(c)}{=} s^{\frac{2}{\alpha}} \Gamma\left(1 - \frac{2}{\alpha}\right) \mathbb{E}\left[W^{\frac{2}{\alpha}}\right] \mathbb{E}\left[\cos^2(\Theta) \times \left(\rho(\Theta) \left(1 - \ell^{\frac{2}{\alpha}}\right) + \ell^{\frac{2}{\alpha}}\right)\right], \end{split}$$

where (c) is acquired by using the two facts that $\mathbb{E}[Y^{-\frac{2}{\alpha}}] = \Gamma(1-\frac{2}{\alpha})$ and $\mathbb{E}[\cos^2(\Theta)L^{\frac{2}{\alpha}}|\Theta] = \cos^2(\Theta)(\rho(\Theta) + [1-\rho(\Theta)]\ell^{\frac{2}{\alpha}})$ for a given Θ . Substituting this result into (A.3) yields the expression in (16).

Next, consider the APDL scenario so that $\Theta_i = \tan^{-1}(H_i/\|X_i\|)$ for all $i \in \mathbb{N}_+$. For this scenario, the integral in (A.3) for a given H can be expressed as

$$\mathbb{P}\left[z \leq \cos^{2}(\Theta) \left(\frac{sWL}{Y}\right)^{\frac{2}{\alpha}} \middle| H\right] = \mathbb{P}\left[Y \leq \frac{sW}{z^{\frac{\alpha}{2}} \sec^{\alpha}(\Theta)} \middle| H\right]
\rho(\Theta) + \mathbb{P}\left[Y \leq \frac{s\ell W}{z^{\frac{\alpha}{2}} \sec^{\alpha}(\Theta)} \middle| H\right] [1 - \rho(\Theta)] = \rho(\Theta)
\times \left[\mathcal{L}_{W} \left(z^{-\frac{\alpha}{2}} s\ell \cos^{\alpha}(\Theta)\right) - \mathcal{L}_{W} \left(z^{-\frac{\alpha}{2}} s \cos^{\alpha}(\Theta)\right)\right]
+ 1 - \mathcal{L}_{W} \left(z^{-\frac{\alpha}{2}} s\ell \cos^{\alpha}(\Theta)\right).$$
(A.4)

We can get the expression in (17) by substituting (A.4) into (A.3).

C. Proof of Theorem 3

In Section II-A, we have pointed out that Φ_u is equivalently equal to a 2D homogeneous PPP of density $\lambda_u = \lambda \mathbb{E}[\cos^2(\Theta)]$ in the APIL scenario. Let U_K denote the Kth nearest point in

 Φ_u to the origin and its projection is X_K . As such, the CCDF of $||U_K||^2$ can be expressed as follows [20], [21], [29]:

$$\mathbb{P}\left[\|U_K\|^2 \ge x\right] = \sum_{k=0}^{K-1} \frac{(\pi \lambda_u x)^k}{k!} e^{-\pi \lambda_u u}$$
$$= \mathbb{P}\left[\|X_K\|^2 \sec^2(\Theta_K) \ge x\right],$$

where Θ_K is the elevation angle of U_K . Thus, the CCDF of $\|U_K\|^2$ reduces to the CCDF of $\|X_K\|^2$ whenever $\Theta_K = 0$ for any K. This follows that

$$\mathbb{P}\left[\|X_K\|^2 \ge x \cos^2(\Theta_K)|\Theta_K = 0\right] = \mathbb{P}\left[\|X_K\|^2 \ge x\right]$$
$$= \sum_{k=0}^{K-1} \frac{(\pi \lambda x)^k}{k!} e^{-\pi \lambda x},$$

which indicates $\|X_K\|^2 \sim \operatorname{Gamma}(K,\pi\lambda)$. For the APDL scenario, Φ_u can be equivalently equal to a 2D non-homogeneous PPP of density $\lambda F_H(\sqrt{z})$, as already shown in Section II-A. As a result, the CCDF of $\|U_K\|^2$ in this scenario can be written as

$$\mathbb{P}\left[\|U_K\|^2 \ge x\right] = \sum_{k=0}^{K-1} \frac{\left[\pi \int_0^x \lambda F_H(\sqrt{z}) dz\right]^k}{e^{\pi \int_0^x \lambda F_H(\sqrt{z}) dz} k!}.$$

Setting H=0 in the above result shows $\|X_K\|^2\sim \mathrm{Gamma}(K,\pi\lambda)$. These above results manifest that the point ordering in Φ_u is the same as that in of the projections of Φ_u that are a homogeneous PPP of density λ_x no matter whether or not the elevation angle and the projection of each point in Φ_u are independent.

Now consider the APIL scenario in which Θ_k and X_k of $U_k \in \Phi_u$ are independent for all $k \in \mathbb{N}_+$. Since U_k is the kth nearest point in Φ_u that is a homogeneous PPP, we know $\|U_{i+K}\|^2 = \|U_K\|^2 + \|U_i\|^2$ where $\|U_K\|$ and $\|U_i\|$ are independent [29], $\mathcal{L}_{T_K}(s)$ can be explicitly expressed as shown in the following:

$$\mathcal{L}_{T_{K}}(s) = \mathbb{E}\left\{\exp\left(-s\sum_{i=1}^{\infty} \frac{W_{i+K}L_{i+K}}{\|U_{i+K}\|^{\alpha}}\right)\right\}$$

$$=\mathbb{E}\left\{\exp\left(-s\sum_{i=1}^{\infty} \frac{W_{i+K}L_{i+K}\cos^{\alpha}(\Theta_{i+K})}{\|X_{K+i}\|^{\alpha}}\right)\right\}$$

$$\stackrel{(a)}{=}\mathbb{E}\left\{\mathbb{E}\left[\prod_{i:X_{i}\in\Phi_{x}}\exp\left(-\frac{sW_{i}L_{i}\cos^{\alpha}(\Theta_{i})}{(\|X_{K}\|^{2}+\|X_{i}\|^{2})^{\frac{\alpha}{2}}}\right)\Big|\|X_{K}\|\right]\right\}$$

$$\stackrel{(b)}{=}\mathbb{E}\left\{\exp\left[-\pi\lambda\int_{0}^{\infty}\left(1-\mathbb{E}\left[\exp\left(-\frac{sWL\cos^{\alpha}(\Theta)}{(\|X_{K}\|^{2}+x)^{\frac{\alpha}{2}}}\right)\right]\right]\right\}$$

$$\stackrel{(c)}{=}\mathbb{E}\left\{\exp\left(-\pi\lambda D_{K}\int_{1}^{\infty}\left\{1-\mathbb{E}_{L,\Theta}\left[\mathcal{L}_{W}\left(\frac{sL\cos^{\alpha}(\Theta)}{z^{\frac{\alpha}{2}}D_{K}^{\frac{\alpha}{2}}}\right)\right]\right\}\right\}$$

$$\left\{dz\right\}\right\},$$
(A.6)

where (a) follows from the fact that all L_i 's $(W_i$'s) are i.i.d. and X_K (X_i) is the projection of U_K (U_i) , (b) is obtained by the PGFL of a 2D homogeneous PPP to Φ_x , and (c) is

obtained by first replacing $||X_K||^2 + x$ with $||X_K||^2z$ in the integral and replacing $||X_K||^2$ with D_K . Also, the integral in (A.6) can be simplified as shown in the following:

$$\begin{split} & \int_{1}^{\infty} \left\{ 1 - \mathbb{E}_{L,\Theta} \left[\mathcal{L}_{W} \left(\frac{sL \cos^{\alpha}(\Theta)}{z^{\frac{\alpha}{2}} D_{K}^{\frac{\alpha}{2}}} \right) \right] \right\} \mathrm{d}z \\ = & \mathbb{E}_{\Theta} \left\{ \rho(\Theta) \int_{1}^{\infty} \left[1 - \mathcal{L}_{W} \left(\frac{s \cos^{\alpha}(\Theta)}{(zD_{K})^{\frac{\alpha}{2}}} \right) \right] \mathrm{d}z \right. \\ & + \left[1 - \rho(\Theta) \right] \int_{1}^{\infty} \left[1 - \mathcal{L}_{W} \left(\frac{s\ell \cos^{\alpha}(\Theta)}{(zD_{K})^{\frac{\alpha}{2}}} \right) \right] \mathrm{d}z \right\}, \end{split}$$

and we can further show

$$\int_{1}^{\infty} \left[1 - \mathcal{L}_{W} \left(x z^{-\frac{\alpha}{2}} \right) \right] dz = \mathcal{I}_{W} \left(x, \frac{2}{\alpha} \right)$$

by following the derivation techniques in the proof of Proposition 1 in [28] and using the definition of $\mathcal{I}_W(x,y)$ in (24). Thus, we finally get the result in (23) owing to $D_K \sim \mathrm{Gamma}(K,\pi\lambda)$.

Now consider the APDL scenario such that $\Theta_i = \tan^{-1}(H_i/\|X_i\|)$. From (A.5),we can rewrite the expression inside the integral with $\Theta = \tan^{-1}(H/\sqrt{\|X_K\|^2 + x})$ and $\|X_K\|^2 + x = D_K + x = z$ as follows:

$$\begin{split} &1 - \mathbb{E}_{L} \left[\mathcal{L}_{W} \left(\frac{sL \cos^{\alpha}(\Theta)}{z^{\frac{\alpha}{2}}} \right) \middle| H \right] = 1 - \rho(\Theta) \\ &\times \mathcal{L}_{W} \left(\frac{s \cos^{\alpha}(\Theta)}{z^{\frac{\alpha}{2}}} \right) - [1 - \rho(\Theta)] \mathcal{L}_{W} \left(\frac{s\ell \cos^{\alpha}(\Theta)}{z^{\frac{\alpha}{2}}} \right) \\ &= \mathcal{J}_{W} \left(\frac{s}{z^{\frac{\alpha}{2}}}, \tan^{-1} \left(\frac{H}{\sqrt{z}} \right) \right). \end{split}$$

Substituting this above result into (A.6) and then averaging the whole expression over $D_K \sim \operatorname{Gamma}(K, \pi \lambda)$ lead to (25). This completes the proof.

D. Proof of Proposition 1

For the APIL scenario, we can infer the following from (27):

$$\min_{i:U_i\in\Phi_u}\{L_i^{-\frac{1}{\alpha}}\|U_i\|\}\stackrel{d}{=}\min_{i:\widetilde{U}_i\in\widetilde{\Phi}_u}\|\widetilde{U}_i\|\triangleq\|\widetilde{U}_\star\|,$$

where $\widetilde{\Phi}_u$ already defined in (12) is a homogeneous PPP of density $\lambda \omega$ as shown in Section II-A and \widetilde{U}_{\star} is the nearest point in $\widetilde{\Phi}_u$ to the origin. Thus, we know

$$\widetilde{I}_0 = \sum_{i:\widetilde{U}_i \in \widetilde{\Phi}_u \backslash \widetilde{U}_\star} PG_i \|\widetilde{U}_i\|^{-\alpha} \stackrel{d}{=} I_0.$$

The CCDF of a non-negative RV Z can be expressed as

$$F_Z^c(z) = \mathcal{L}^{-1}\left\{\frac{1}{s}\mathcal{L}_{Z^{-1}}\left(s\right)\right\}\left(\frac{1}{z}\right), \ s > 0. \tag{A.7}$$

It can be used to express p_{cov} in (30) for $G_i \sim \exp(1)$ as follows:

$$\begin{split} p_{cov} = & \mathcal{L}^{-1} \left\{ \frac{1}{s} \mathcal{L}_{\gamma_0^{-1}}(s) \right\} \\ = & \mathcal{L}^{-1} \left\{ \mathbb{E} \left[\frac{1}{s} \exp \left(-s \frac{(\widetilde{I}_0 + \sigma_0) \|U_\star\|^\alpha}{PG_\star L_\star} \right) \right] \right\} \left(\frac{1}{\beta} \right) \\ = & \mathcal{L}^{-1} \left\{ \mathbb{E} \left[\frac{1}{s} \exp \left(-\frac{s\sigma_0 \|\widetilde{U}_\star\|^\alpha}{PG_\star} \right) \right] \right\} \left(\frac{1}{\beta} \right) \\ & \times \mathcal{L}_{\widetilde{I}_0 | \|\widetilde{U}_\star\|} \left(\frac{s \|\widetilde{U}_\star\|^\alpha}{PG_\star} \right) \right] \right\} \left(\frac{1}{\beta} \right), \end{split} \tag{A.8}$$

where $\mathcal{L}_{\widetilde{I}_0||\widetilde{U}_{\star}||}(\cdot)$ is the Laplace transform of \widetilde{I}_0 while conditioning on $\|\widetilde{U}_{\star}\|$. Note that \widetilde{I}_0 is the first-truncated shot signal process in $\widetilde{\Phi}_u$ since the projection of point \widetilde{U}_{\star} is the nearest point among all the projections of the points in $\widetilde{\Phi}_u$, that is, \widetilde{I}_0 is equal to T_K in (22) for K=1, $W_k=PG_k$, and $L_k=1$.

Since I_0 is the first-truncated shot signal process in Φ_u , W=PG, and $\|\widetilde{U}_\star\|^2=D_\star\sim\exp(\pi\lambda\omega)$, $\mathcal{L}_{\widetilde{I}_0|\|\widetilde{U}_\star\|}(\cdot)$ in (A.8) can be found by using K=1 and replacing s with $s\|\widetilde{U}_\star\|^\alpha/PG_\star$ in (23) as follows

$$\begin{split} \mathcal{L}_{\widetilde{I}_{0}\mid\parallel\widetilde{U}_{\star}\parallel}\left(\frac{s\|\widetilde{U}_{\star}\|^{\alpha}}{PG_{\star}}\right) &= \exp\left[-\pi\lambda\omega D_{\star}\mathcal{I}_{W}\left(\frac{s}{PG_{\star}},\frac{2}{\alpha}\right)\right] \\ &= \exp\left[-\pi\lambda\omega D_{\star}\mathcal{I}_{G}\left(\frac{s}{G_{\star}},\frac{2}{\alpha}\right)\right], \end{split}$$

where $\mathcal{I}_W(s/PG_{\star}, 2/\alpha)$ for W = PG and $G \sim \exp(1)$ is equal to $\mathcal{I}_G(s/G_{\star}, 2/\alpha)$ defined in (32). Then substituting this result into (A.8) yields

$$p_{cov} = \mathcal{L}^{-1} \left\{ \mathbb{E} \left[\frac{1}{s} \exp \left(-\frac{s\sigma_0 D_{\star}^{\frac{\alpha}{2}}}{PG} - \pi \lambda \omega D_{\star} \right) \right] \right\} \left(\frac{s}{G_{\star}}, \frac{2}{\alpha} \right) \right\} \left(\frac{1}{\beta} \right). \tag{A.9}$$

Furthermore, we know the following identity for a real-valued function $\psi : \mathbb{R}_+ \to \mathbb{R}_+$:

$$\mathbb{E}\left\{\frac{1}{s}\exp\left[-\psi\left(\frac{s}{Z}\right)\right]\right\} = \int_0^\infty \exp\left[-\psi\left(\frac{1}{t}\right)\right] f_Z(st) dt,$$
(A.10)

where $f_Z(z)$ is the PDF of Z. This follows that

$$\mathbb{E}\left[\frac{1}{s}\exp\left(-\frac{s\sigma_{0}D_{\star}^{\frac{\alpha}{2}}}{PG_{\star}} - \pi\lambda\omega D_{\star}\mathcal{I}_{G}\left(\frac{s}{G_{\star}}, \frac{2}{\alpha}\right)\right)\right] =$$

$$\int_{0}^{\infty}\exp\left[-\frac{\sigma_{0}D_{\star}^{\frac{\alpha}{2}}}{Pt} - \pi\lambda\omega D_{\star}\mathcal{I}_{G}\left(\frac{1}{t}, \frac{2}{\alpha}\right)\right]f_{G_{\star}}(st)dt$$

$$\stackrel{(a)}{=}\frac{1}{(N-1)!}\int_{0}^{\infty}\exp\left[-\frac{\sigma_{0}D_{\star}^{\frac{\alpha}{2}}}{Pt} - \pi\lambda\omega D_{\star}\mathcal{I}_{G}\left(\frac{1}{t}, \frac{2}{\alpha}\right)\right]$$

$$(st)^{N-1}e^{-st}dt\stackrel{(b)}{=}\frac{s^{N-1}}{(N-1)!}\int_{0}^{\infty}\exp\left[-\frac{\sigma_{0}D_{\star}^{\frac{\alpha}{2}}}{Pt} - \pi\lambda\omega\right]$$
(A 11)

$$\times D_{\star} \mathcal{I}_{G} \left(\frac{1}{t}, \frac{2}{\alpha} \right) \right] t^{N-1} e^{-st} dt = \mathcal{L} \left\{ \frac{1}{(N-1)!} \frac{d^{N-1}}{dt^{N-1}} \right.$$

$$\left[t^{N-1} \exp \left(-\frac{\sigma_{0} D_{\star}^{\frac{\alpha}{2}}}{Pt} - \pi \lambda \omega D_{\star} \mathcal{I}_{G} \left(\frac{1}{t}, \frac{2}{\alpha} \right) \right) \right] \right\} (s),$$
(A.12)

where (a) is obtained due to $G_{\star} \sim \operatorname{Gamma}(N,1)$ and (b) is obtained by moving s^{N-1} out of the integral. We then substitute (A.12) into (A.9) to get p_{cov} as shown in (31).

E. Proof of Proposition 2

By letting $S_0 \triangleq \sum_{i:U_i \in \Phi_u} G_i L_i \|U_i\|^{-\alpha}$ and using (A.7), the cell-free downlink coverage defined in (37) can be rewritten as

$$p_{cov}^{cf} = 1 - \mathbb{P}\left[S_0 \le \frac{\beta\sigma_0}{P}\right] = 1 - F_{S_0}^c \left(\frac{P}{\beta\sigma_0}\right)$$
$$= 1 - \mathcal{L}^{-1}\left\{\frac{1}{s}\mathcal{L}_{S_0}(s)\right\}\left(\frac{\beta\sigma_0}{P}\right). \tag{A.13}$$

Note that $S_0 \stackrel{d}{=} T_0$ defined in (15) with $G_i = W_i$ so that S_0 is a Poisson shot signal process in Φ_u . According to Theorem 2, $\mathcal{L}_{S_0}(s) = \mathcal{L}_{I_0}(s)$ for $W \sim \operatorname{Gamma}(N,1)$ can be found as

$$\mathcal{L}_{S_0}(s) = \exp\left\{-\pi \lambda s^{\frac{2}{\alpha}} \mathbb{E}\left[W^{\frac{2}{\alpha}}\right] \Gamma\left(1 - \frac{2}{\alpha}\right) \omega\right\}$$
$$= \exp\left[-\frac{\pi \lambda s^{\frac{2}{\alpha}} \omega}{(N-1)!} \Gamma\left(N + \frac{2}{\alpha}\right) \Gamma\left(1 - \frac{2}{\alpha}\right)\right].$$

Substituting this into (A.13) leads to (38). For $\alpha = 4$, (38) further reduces to (39) since the inverse Laplace transform can be found in closed form [27].

F. Proof of Proposition 3

Since the APDL scenario is considered, we know $\widetilde{\Phi}_u$ is a 2D non-homogeneous PPP of density $\lambda \frac{\mathrm{d}\Omega(y^{\frac{\alpha}{2}})}{\mathrm{d}y}$ with $\Omega(y^{\alpha/2})$ given in (14), as shown in Section II-A. Moreover, \widetilde{I}_0 is the first-truncated shot signal process in $\widetilde{\Phi}_u$, as pointed out in Appendix E. We thus are able to express $\mathcal{L}_{\widetilde{I}_0|\|\widetilde{U}_{\star}\|}(\cdot)$ in (A.8) by using $K=1, W=PG, G\sim \exp(1), L=1$, and replacing D_K with $\|\widetilde{U}_{\star}\|^2=\widetilde{D}_{\star}$ in (25) as follows:

$$\begin{split} &\mathcal{L}_{\widetilde{I}_{0}|\|\widetilde{U}_{\star}\|}\left(\frac{s\|\widetilde{U}_{\star}\|^{\alpha}}{PG_{\star}}\right) \\ &= \mathbb{E}\left[\exp\left(-\frac{s\widetilde{D}_{\star}^{\frac{\alpha}{2}}}{G_{\star}}\sum_{i:\widetilde{U}_{i}\in\widetilde{\Phi}_{u}\backslash\widetilde{U}_{\star}}\frac{G_{i}}{(\widetilde{D}_{\star}+\|\widetilde{U}_{i}\|^{2})^{\frac{\alpha}{2}}}\right)\right] \\ &\stackrel{(a)}{=}\exp\left[-\pi\lambda\int_{\widetilde{D}_{\star}}^{\infty}\left[\frac{\mathrm{d}\Omega\left(y^{-\frac{\alpha}{2}}\right)}{\mathrm{d}y}\right]\mathcal{J}_{W}\left(\frac{s\widetilde{D}_{\star}^{\frac{\alpha}{2}}}{G_{\star}y^{\frac{\alpha}{2}}},0\right)\mathrm{d}y\right] \\ &\stackrel{(b)}{=}\exp\left[-\pi\lambda\widetilde{D}_{\star}\int_{1}^{\infty}\left(\frac{s}{G_{\star}y^{\frac{\alpha}{2}}+s}\right)\mathrm{d}\Omega\left(\frac{\widetilde{D}_{\star}}{y^{\frac{\alpha}{2}}}\right)\right], \quad (A.14) \end{split}$$

where (a) is obtained by applying the result in (25) for $\widetilde{\Phi}_u$ and K=1 and then assuming $\widetilde{\Theta}_\star=\tan^{-1}\frac{H}{\sqrt{y\widetilde{D}_\star}}$ is the elevation

angle between the typical user and \widetilde{U}_{\star} , and (b) is because $\mathcal{J}_W(\cdot,\cdot)$ in (18) for W=G and $\ell=1$ can be expressed as

$$\mathcal{J}_W\left(\frac{s}{G_{\star}y^{\frac{\alpha}{2}}},0\right) = 1 - \mathcal{L}_G\left(\frac{s}{G_{\star}y^{\frac{\alpha}{2}}}\right) = \frac{s}{G_{\star}y^{\frac{\alpha}{2}} + s}.$$

Substituting (A.14) into (A.8) and following the steps of deriving (A.12) yield the result in (42).

REFERENCES

- Paving the path to 5G: Optimizing commercial LTE networks for drone communication. [Online]. Available: https://www.qualcomm.com/news/onq/2016/09/06/paving-path-5goptimizing-commercial-lte-networks-drone-communication
- [2] D. Schneider, "Air traffic control for delivery drones," *IEEE Spectrum*, pp. 32–33, Jan. 2017.
- [3] M. M. Azari, F. Rosas, K.-C. Chen, and S. Pollin, "Ultra reliable UAV communication using altitude and cooperation diversity," *IEEE Trans. Commun.*, vol. 66, no. 1, pp. 330–344, Jan. 2018.
- [4] S. Yang, Y. Deng, X. Tang, Y. Ding, and J. Zhou, "Energy efficiency optimization for UAV-assisted backscatter communications," *IEEE Commun. Lett.*, vol. 23, no. 11, pp. 2041–2045, Nov. 2019.
- [5] Z. Wang, L. Duan, and R. Zhang, "Adaptive deployment for UAV-aided communication networks," *IEEE Trans. Commun.*, vol. 18, no. 9, pp. 4531–4543, Sep. 2019.
- [6] Y. Zeng and R. Zhang, "Energy-efficient UAV communication with trajectory optimization," *IEEE Trans. Wireless Commun.*, vol. 16, no. 6, pp. 3747–3760, Jun. 2017.
- [7] F. Ono, H. Ochiai, and R. Miura, "A wireless relay network based on unmanned aircraft system with rate optimization," *IEEE Trans. Wireless Commun.*, vol. 15, no. 11, pp. 7699–7708, Nov. 2016.
- [8] X. Yuan, Z. Feng, W. Xu, W. Ni, J. A. Zhang, Z. Wei, and R. P. Liu, "Capacity analysis of UAV communications: Cases of random trajectories," *IEEE Trans. Veh. Technol.*, vol. 67, no. 8, pp. 7564–7576, Aug. 2018.
- [9] V. V. Chetlur and H. S. Dhillon, "Downlink coverage analysis for a finite 3-D wireless network of unmanned aerial vehicles," *IEEE Trans. Commun.*, vol. 65, no. 10, pp. 4543–4558, Oct. 2017.
- Commun., vol. 65, no. 10, pp. 4543–4558, Oct. 2017.

 [10] T. Hou, Y. Liu, Z. Song, X. Sun, and Y. Chen, "Exploiting NOMA for UAV communications in large-scale cellular networks," *IEEE Trans. Commun.*, vol. 67, no. 10, pp. 6897–6911, Oct. 2019.
- Commun., vol. 67, no. 10, pp. 6897–6911, Oct. 2019.
 Y. Sun, Z. Ding, and X. Dai, "A user-centric cooperative scheme for UAV-assisted wireless networks in malfunction areas," *IEEE Trans. Commun.*, vol. 67, no. 12, pp. 8786–8800, Dec. 2019.
- [12] D. Kim, J. Lee, and T. Q. Quek, "Multi-layer unmanned aerial vehicle networks: Modeling and performance analysis," *IEEE Trans. Wireless Commun.*, vol. 19, no. 1, pp. 325–339, Jan. 2020.
- [13] M. M. Azari, G. Geraci, A. Garcia-Rodriguez, and S. Pollin, "UAV-to-UAV communications in cellular networks," *IEEE Trans. Wireless Commun.*, Early Access 2020.
- [14] J. Yao and J. Xu, "Secrecy transmission in large-scale UAV-enabled wireless networks," *IEEE Trans. Commun.*, vol. 67, no. 11, pp. 7656– 7671, Nov. 2019.
- [15] B. Galkin, J. Kibilda, and L. A. DaSilva, "Coverage analysis for low-altitude UAV networks in urban environments," in *IEEE Global Communications Conference (Globecom)*, Dec. 2017, pp. 1–6.
- [16] B. Shang, L. Liu, R. M. Rao, V. Marojevic, and J. H. Reed, "3D spectrum sharing for hybrid D2D and UAV networks," *IEEE Trans. Commun.*, Early Access 2020.
- [17] C.-H. Liu, K.-H. Ho, and J.-Y. Wu, "Mmwave UAV networks with multicell association: Performance limit and optimization," *IEEE J. Sel. Areas Commun.*, vol. 37, no. 12, pp. 2814–2831, Dec. 2019.
- [18] T. Hou, Y. Liu, Z. Song, X. Sun, and Y. Chen, "UAV-to-everything (U2X) networks relying on NOMA: A stochastic geometry model," *IEEE Trans. Veh. Technol.*, vol. 69, no. 7, pp. 7558–7568, Jul. 2020.
- [19] C. Zhang and W. Zhang, "Spectrum sharing for drone networks," IEEE J. Sel. Areas Commun., vol. 35, no. 1, pp. 136–144, Jan. 2017.
- [20] S. N. Chiu, D. Stoyan, W. S. Kendall, and J. Mecke, Stochastic Geometry and Its Applications, 3rd ed. New York: John Wiley and Sons, Inc., 2013.
- [21] M. Haenggi, Stochastic Geometry for Wireless Networks, 1st ed. Cambridge University Press, 2012.
- [22] A. Al-Hourani, S. Kandeepan, and S. Lardner, "Optimal LAP altitude for maximum coverage," *IEEE Wireless Commun. Lett.*, vol. 3, no. 6, pp. 569–572, Dec. 2014.

- [23] W. Yi, Y. Liu, Y. Deng, and A. Nallanathan, "Clustered UAV networks with millimeter wave communications: A stochastic geometry view," *IEEE Trans. Commun.*, vol. 68, no. 7, pp. 4342–4357, Jul. 2020.
- [24] S. B. Lowen and M. C. Teich, "Power-law shot noise," *IEEE Trans. Inf. Theory*, vol. 36, no. 6, pp. 1302–1318, Sep. 1990.
- [25] C.-H. Liu and H.-M. Hu, "Full-duplex heterogeneous networks with decoupled user association: Rate analysis and traffic scheduling," *IEEE Trans. Commun.*, vol. 67, no. 3, pp. 2084–2100, Mar. 2019.
- [26] C.-H. Liu, "Coverage-rate tradeoff analysis in mmwave heterogeneous cellular networks," *IEEE Trans. Commun.*, vol. 67, no. 2, pp. 1720–1736, Feb. 2019.
- [27] M. Abramowitz and I. A. Stegun, Handbook of mathematical functions: with formulas, graphs, and mathematical tables. Courier Dover Publications, 2012.
- [28] C.-H. Liu and L.-C. Wang, "Random cell association and void probability in poisson-distributed cellular networks," in *IEEE Int. Conf. on Commun. (ICC)*, Jun. 2015, pp. 2816–2821.
- [29] ——, "Optimal cell load and throughput in green small cell networks with generalized cell association," *IEEE J. Sel. Areas Commun.*, vol. 34, no. 5, pp. 1058–1072, May 2016.
- [30] H. S. Dhillon, M. Kountouris, and J. G. Andrews, "Downlink MIMO hetnets: Modeling, ordering results and performance analysis," *IEEE Trans. Wireless Commun.*, vol. 12, no. 10, pp. 5208–5222, Oct. 2013.
- [31] P. Xia, C.-H. Liu, and J. G. Andrews, "Downlink coordinated multipoint with overhead modeling in heterogeneous cellular networks," *IEEE Trans. Wireless Commun.*, vol. 12, no. 8, pp. 4025–4037, Aug. 2013.
- [32] D. Lee, H. Seo, B. Clerckx, E. Hardouin, D. Mazzarese, S. Nagata, and K. Sayana, "Coordinated multipoint transmission and reception in LTE-Advanced: Deployment scenarios and operational challenges," *IEEE Commun. Mag.*, vol. 50, no. 2, pp. 148–155, Feb. 2012.
- [33] R. Tanbourgi, S. Singh, J. G. Andrews, and F. K. Jondral, "A tractable model for noncoherent joint-transmission base station cooperation," *IEEE Trans. Wireless Commun.*, vol. 13, no. 9, pp. 4959–4973, Sep. 2014.



Md Asif Syed was born in Khulna, Bangladesh. He received the B.Sc. degree in Electronics and Communication Engineering from Khulna University, Bangladesh, in 2009, and the M.E. degree from Inha University, South Korea, in 2015. He is currently pursuing his Ph.D. degree in the Department of Electrical and Computer Engineering, Mississippi State University, Starkville, MS, USA. His current research interests include intelligent reflecting surface (IRS), unmanned aerial vehicle (UAV) communications, and stochastic geometry.



Chun-Hung Liu (Senior Member, IEEE) received the B.S. degree in Mechanical Engineering from National Taiwan University, Taipei, Taiwan, the M.S. degree in Mechanical Engineering from Massachusetts Institute of Technology, Cambridge MA, USA, and the Ph.D. degree in electrical and computer engineering from The University of Texas at Austin, TX, USA. He is currently an Assistant Professor with the Department of Electrical and Computer Engineering at Mississippi State University, Starkville MS, USA. He was with the University of

Michigan, Ann Arbor MI, USA and National Chiao Tung University, Hsinchu, Taiwan. His research interests include wireless communication, information theory, stochastic geometry and random graph, machine learning, control and optimization theory. He was a recipient of the Best Paper Award from IEEE Global Communications Conference (Globecom) in 2008 and 2014, a recipient of the Excellent Young Researcher Award from the Ministry of Science and Technology of Taiwan in 2015, a recipient of the Outstanding Advisor Award from the Taiwan Institute of Electrical and Electronic Engineering in 2016.



Rung-Hung Gau (Senior Member, IEEE) received the B.S. degree in electrical engineering from National Taiwan University, Taipei, Taiwan, the M.S. degree in electrical engineering from University of California at Los Angeles, Los Angeles, CA, USA, and the Ph.D. degree in electrical and computer engineering from Cornell University, Ithaca, NY, USA, in 1994, 1997, and 2001, respectively. He is currently a professor and the director of the Institute of Communications Engineering, National Chiao Tung University, Hsinchu, Taiwan. His current

research interests include optimal resource allocation in NOMA wireless networks, machine learning and optimization for wireless communications and mobile computing, UAV communication networks, Internet of things, and software defined networking.



Di-Chun Liang received the B.S. degree in Electrical and Eomputer Engineering from National Chiao Tung University (NCTU), Hsinchu, Taiwan, in 2013. He is currently a Ph.D. candidate in the Institute of Communications Engineering and the Department of Electrical and Computer Engineering at NCTU. His research interests include wireless communications, stochastic geometry, and machine learning.